

Chiral enhancement of two-magnon bound states in an $S = 1/2$ triangular-lattice magnet

László Rudner^{1,2} and Karlo Penc²

¹*Department of Theoretical Physics, Institute of Physics,
Budapest University of Technology and Economics,
Műgyetem rakpart 3, H-1111 Budapest, Hungary*

²*HUN-REN Wigner Research Centre for Physics,
Institute for Solid State Physics and Optics, Budapest, Hungary*

(Dated: July 2, 2026)

We study one- and two-magnon excitations above the fully polarized state of the spin-1/2 triangular-lattice J_1 - J_2 - J_3 Heisenberg model with an additional uniform scalar-chirality interaction. In the one-magnon sector of the Heisenberg model, we identify two special minimum manifolds by rewriting the dispersion in complete-square form. The scalar-chirality term cancels exactly in this sector, leaving the one-magnon dispersion and the single-magnon instability unchanged. In contrast, it survives in the two-magnon sector as an oriented interaction between neighboring flipped spins. Using symmetry-adapted triangular-lattice harmonics, we derive finite-dimensional gap equations at the Γ point in the symmetry-resolved A_1 and E_2 -type partial-wave channels. The chirality coupling splits the two opposite relative-motion chiralities in the E_2 -type sector, thereby selectively enhancing one two-magnon bound-state channel. Exact diagonalization confirms this mechanism and reveals enhanced binding, as well as additional bound states at M and at incommensurate total momenta. Our results identify scalar chirality as an efficient microscopic mechanism for strengthening two-magnon binding without shifting the one-magnon spectrum, and provide a route toward high-field spin-nematic and multipolar instabilities.

I. INTRODUCTION

In a conventional magnetically ordered state, spin-rotational symmetry is broken by a dipolar order parameter, i.e., by a finite expectation value of the spin operators themselves. Quantum magnets can also support more subtle forms of symmetry breaking in which dipolar order is absent and higher-rank multipolar order is realized instead. The simplest such case is spin-nematic order, where spin rotations are broken by quadrupolar correlations rather than by a finite magnetic moment. For $S = 1$ moments, quadrupolar order can arise directly from local spin degrees of freedom, whereas in spin-1/2 systems nematic order corresponds to long-range order in inter-site spin-bilinear operators [1, 2]. In this sense, spin-nematic order is the two-particle analog of conventional magnon condensation: instead of single magnons condensing, bound two-magnon states condense while single-magnon excitations remain gapped [3, 4]. For $S = 1/2$, frustrated magnets with competing ferromagnetic nearest-neighbor and antiferromagnetic next-nearest-neighbor exchange interactions provide natural settings for this mechanism, as illustrated by the one-dimensional zigzag chain, where quasi-long-range multipolar correlations appear [5–9], and by two-dimensional square-lattice models [10–12]. In these systems, frustration can generate an effective attraction between magnons, allowing a two-magnon bound state to soften and condense before the single-magnon mode becomes unstable.

The high-field regime provides a particularly clean way to formulate this problem. Above the saturation field, the fully polarized state is an exact vacuum, a flipped

spin is a magnon, and the leading instability upon lowering the field is determined by the few-magnon spectrum above this vacuum. If the lowest excitation is a single magnon, its condensation produces conventional transverse dipolar order. If, instead, the lowest excitation is a two-magnon bound state, its condensation signals a spin-nematic instability, with an order parameter of the form $\langle S_i^- S_j^- \rangle$ for spin-1/2 systems. This viewpoint also makes clear that the mere existence of a two-magnon bound state is not sufficient to establish a stable nematic phase. One must determine whether the bound state preempts single-magnon condensation and whether it remains stable against competing many-body or higher-multipolar instabilities. Recent work on square-lattice ferro-antiferromagnets has emphasized this point, showing that the parameter window for nematic order can be strongly constrained once the full high-field phase diagram is considered [12].

Experimental evidence for spin-nematic phases remains scarce, despite the existence of several candidate materials [13–23]. A central difficulty is that spin-nematic order is encoded in quadrupolar, rather than dipolar, correlations. As a result, the relevant quadrupolar excitations couple only weakly to probes that primarily measure single-spin, dipolar correlations.

Nevertheless, several spectroscopic routes can provide indirect access to two-magnon bound states and related quadrupolar correlations. Inelastic neutron scattering couples primarily to dipolar spin fluctuations, but magnon-pair excitations can leave signatures in multiparticle continua and in the dynamics of spin-nematic phases [24–26]. Light scattering provides a complementary probe. In Mott-Hubbard insulators, the effective

Raman operator contains the Fleury-Loudon bilinear exchange term at leading order, while higher-order resonant processes generate nonlocal and multispin vertices [27]. These vertices can carry spectral weight in quadrupolar and two-magnon channels [28]; on lattices with triangular loops, they can also include three-spin chiral Raman operators [29]. RIXS further extends this logic by allowing symmetry-selected probes of hidden multipolar order, including spin-nematic and scalar-chirality correlations [30]. Recent experiments on Y_2BaNiO_5 , Sr_2IrO_4 , and $\text{Sr}_2\text{CoGe}_2\text{O}_7$ illustrate how RIXS, Raman, resonant diffraction, and electric-dipole-active spectroscopy can reveal quadrupolar or spin-nematic correlations beyond conventional single-magnon probes [31–34].

The triangular lattice is a natural setting in which to revisit the two-magnon problem. It is the simplest two-dimensional lattice with strong geometric frustration, and its elementary triangular plaquettes support a scalar spin chirality

$$\chi_{ijk} = \mathbf{S}_i \cdot (\mathbf{S}_j \times \mathbf{S}_k), \quad (1)$$

which is invariant under global spin rotations but odd under time reversal and mirror reflection. Scalar spin chirality plays a central role in theories of chiral spin liquids and related topological magnetic phases [35]. On the triangular lattice, chiral interactions and chiral correlations have been studied in extended spin models and Hubbard-derived models, including spin scalar chirality perturbations that stabilize Kalmeyer–Laughlin-type chiral spin liquids [36], triangular-lattice Hubbard models with chiral spin-liquid phases [37, 38], and four-spin exchange mechanisms proposed to generate such phases in Mott insulators [39].

The same lattice also supports a broad range of multipolar magnetic orders. For example, spin-1/2 triangular-lattice models with multiple-spin exchange interactions, motivated in part by thin films of solid ^3He , may support octupolar, or triatic, order [40] as well as octahedral spin-nematic order [41]. Spin-1 models with biquadratic exchange exhibit quadrupolar phases [42–44]. On the materials side, the triangular antiferromagnet NiGa_2S_4 has long motivated spin-nematic scenarios [43–45], while recent experiments on the spin-1 triangular-lattice compound $\text{Na}_2\text{BaNi}(\text{PO}_4)_2$ report signatures of two-magnon bound-state condensation and quadrupolar excitations [46, 47]. These results show that the triangular lattice is a platform on which two-magnon, three-magnon, and more general multipolar instabilities arise naturally. They raise a basic question: how does scalar spin chirality affect the formation, symmetry, and stability of two-magnon bound states on the triangular lattice?

Here we address this question in the high-field limit of a spin-1/2 triangular-lattice model with exchange interactions and a uniform scalar-chirality term. We focus on the one- and two-magnon sectors above the fully polarized state. This setting isolates a particularly transparent effect of the scalar-chirality interaction. As we show explicitly below, for the uniform chirality pattern

considered here, the scalar-chirality term does not modify the one-magnon dispersion: the hopping amplitudes generated by the two elementary triangles sharing a bond cancel in the fully polarized background. Consequently, the one-magnon critical field and the location of the one-magnon minima are unchanged at the single-particle level. In the two-magnon sector, however, this cancellation is no longer complete when the two flipped spins occupy neighboring sites. The scalar-chirality term therefore enters the two-magnon interaction vertex directly, where it can modify the binding energy, distinguish clockwise from counterclockwise relative motion, and lift the degeneracy of a two-dimensional partial-wave channel by splitting it into opposite-chirality components. We find that the chirality interaction selectively enhances binding in one of these chiral components.

The two-magnon calculation serves as the first step in a hierarchy of few-body diagnostics. A two-magnon bound state is the necessary precursor of a quadrupolar spin-nematic instability near saturation, but it may compete with bound states of three or more magnons associated with more general multipolar orders. This point is especially important on the $S = 1/2$ triangular lattice, where multiple-spin exchange models are already known to stabilize the triatic and octahedral-nematic orders mentioned above. Thus, our analysis identifies the leading pair channels and their chiral structure, which is a necessary ingredient for any subsequent many-body treatment.

The remainder of this manuscript is organized as follows. Section II defines the spin-1/2 triangular-lattice model, including the Heisenberg exchanges, the scalar-chirality interaction, and the lattice conventions. In Sec. III, we revisit the Luttinger–Tisza phase diagram of the Heisenberg model and identify special one-magnon minimum manifolds using complete-square decompositions of the dispersion. Section IV analyzes the one-magnon sector above the fully polarized state and shows how the scalar-chirality term cancels from the single-magnon dispersion. Section V derives the two-magnon Schrödinger equation, the scalar-chirality contribution to the two-magnon interaction kernel, and the corresponding gap equation for bound states. The resulting bound-state spectra, binding energies, and dominant partial-wave channels are presented in Sec. VI. Finally, Sec. VII summarizes the main results and discusses their implications for high-field spin-nematic and multipolar instabilities.

II. THE SPIN HAMILTONIAN

We consider the spin-1/2 Hamiltonian

$$\hat{H} = \hat{H}_{\text{Heis}} + \hat{H}_{\text{Chir}} + \hat{H}_{\text{Zeem}}. \quad (2)$$

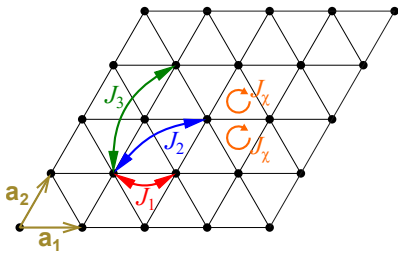


FIG. 1. Triangular lattice showing the J_1 first-, J_2 second-, and J_3 third-neighbor Heisenberg exchanges, as well as the scalar-chirality terms $\hat{\chi}_{ijk}$ on the up- and down-pointing triangles. The circular arrows define the orientation of the ordered sites i , j , and k around each triangle. The primitive lattice vectors are $\mathbf{a}_1 = (1, 0)$ and $\mathbf{a}_2 = (1/2, \sqrt{3}/2)$.

The Heisenberg part is

$$\begin{aligned} \hat{H}_{\text{Heis}} = & \frac{J_1}{2} \sum_{\mathbf{r}} \sum_{\mu=1}^6 \hat{\mathbf{S}}_{\mathbf{r}} \cdot \hat{\mathbf{S}}_{\mathbf{r}+\delta_{\mu}^{(1)}} \\ & + \frac{J_2}{2} \sum_{\mathbf{r}} \sum_{\mu=1}^6 \hat{\mathbf{S}}_{\mathbf{r}} \cdot \hat{\mathbf{S}}_{\mathbf{r}+\delta_{\mu}^{(2)}} \\ & + \frac{J_3}{2} \sum_{\mathbf{r}} \sum_{\mu=1}^6 \hat{\mathbf{S}}_{\mathbf{r}} \cdot \hat{\mathbf{S}}_{\mathbf{r}+\delta_{\mu}^{(3)}}. \end{aligned} \quad (3)$$

Here \mathbf{r} runs over all lattice sites. The vectors $\delta_{\mu}^{(n)}$ connect a site to its n th-neighbor sites, as defined in Eqs. (A2)–(A4). Each shell contains six bond vectors, and the factor $1/2$ removes the double counting of bonds. For $S = 1/2$, the exchange operator can be written in terms of the two-site permutation operator \hat{P}_{ij} as

$$\hat{\mathbf{S}}_i \cdot \hat{\mathbf{S}}_j = \frac{1}{2} \hat{P}_{ij} - \frac{1}{4}. \quad (4)$$

The scalar-chirality term is

$$\hat{H}_{\text{Chir}} = 4J_{\chi} \sum_{\langle ijk \rangle_{\Delta, \nabla}} \hat{\chi}_{ijk}, \quad (5)$$

with

$$\hat{\chi}_{ijk} = \hat{\mathbf{S}}_i \cdot (\hat{\mathbf{S}}_j \times \hat{\mathbf{S}}_k). \quad (6)$$

The sum runs over elementary up- and down-pointing triangles, with the orientation of the ordered triplets $\langle ijk \rangle_{\Delta, \nabla}$ fixed by the circular arrows in Fig. 1. Reversing this orientation changes the sign of $\hat{\chi}_{ijk}$. For spin- $1/2$, the scalar chirality can equivalently be written as the oriented antisymmetric part of the cyclic three-site permutation,

$$\hat{\chi}_{ijk} = \frac{i}{4} (\hat{P}_{ijk} - \hat{P}_{kji}), \quad (7)$$

where \hat{P}_{ijk} cyclically permutes the spins as $i \rightarrow j \rightarrow k \rightarrow i$, while $\hat{P}_{kji} = \hat{P}_{ijk}^{-1}$ denotes the opposite cyclic

orientation. With the normalization chosen in Eq. (5), the chirality Hamiltonian may therefore also be written as

$$\hat{H}_{\text{Chir}} = iJ_{\chi} \sum_{\langle ijk \rangle_{\Delta, \nabla}} (\hat{P}_{ijk} - \hat{P}_{kji}). \quad (8)$$

Such a term arises at the third order in the strong-coupling expansion of a Hubbard model, when the electron hopping amplitudes acquire a nonzero gauge-invariant Peierls phase around a triangular plaquette, equivalently a finite flux through the plaquette [48, 49]. The scalar chirality is odd under time reversal and under the point group operations that reverse the orientation of the triangle. Hence, a uniform scalar-chirality coupling preserves the proper sixfold rotations but removes the orientation-reversing spatial symmetries. In terms of planar point groups, or rosette groups, this reduces the spatial symmetry from the dihedral group D_6 to the cyclic group C_6 .

Finally, the Zeeman term is

$$\hat{H}_{\text{Zeem}} = -h \sum_{\mathbf{r}} \hat{S}_{\mathbf{r}}^z, \quad (9)$$

corresponding to an external magnetic field along the z axis. Both \hat{H}_{Heis} and \hat{H}_{Chir} are $SU(2)$ symmetric, whereas \hat{H}_{Zeem} reduces the spin-rotation symmetry to $U(1)$.

III. LUTTINGER–TISZA PHASE BOUNDARIES AND THE SINGLE MAGNON DISPERSION

The triangular-lattice Heisenberg model has long served as a minimal setting for frustration-induced magnetic order. For the triangular-lattice J_1 - J_2 - J_3 Heisenberg model, variational classifications in terms of regular and spiral states have been given for both antiferromagnetic and ferromagnetic nearest-neighbor exchange [50]. More recent Luttinger–Tisza and numerical work has emphasized the antiferromagnetic regime and its commensurate, incommensurate, and spiral-spin-liquid phases, including the special degenerate line $J_2 = 2J_3$ [51]. Ferromagnetic nearest-neighbor exchange with frustrating further-neighbor interactions has also been studied in the context of frustration-induced skyrmion and anti-skyrmion crystals [52, 53].

A. Luttinger–Tisza phase diagram of the Heisenberg model

For a Bravais lattice with isotropic exchange, the Luttinger–Tisza method reduces the classical ordering problem to minimizing the Fourier-transform of the exchange interaction

$$\mathcal{J}_{\mathbf{q}} = 6J_1\gamma_{\mathbf{q}}^{(1)} + 6J_2\gamma_{\mathbf{q}}^{(2)} + 6J_3\gamma_{\mathbf{q}}^{(3)}. \quad (10)$$

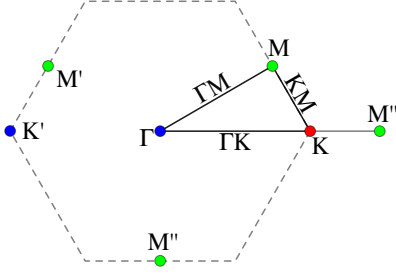


FIG. 2. Brillouin zone of the triangular lattice with the inequivalent Γ , K , and M points and high-symmetry lines. We also illustrate the $\mathbf{q} = (q, 0)$ line in Eq. (23) that connect Γ , K , and M'' point in straight line.

over the Brillouin zone. The $\gamma_{\mathbf{q}}^{(n)}$ above are the lattice harmonics defined in Appendix A, Eqs. (A6). Explicitly, $\mathcal{J}_{\mathbf{q}}$ takes the form

$$\begin{aligned} \mathcal{J}_{\mathbf{q}} = & 2J_1 \left[\cos q_x + 2 \cos \frac{q_x}{2} \cos \frac{\sqrt{3}q_y}{2} \right] \\ & + 2J_2 \left[\cos(\sqrt{3}q_y) + 2 \cos \frac{3q_x}{2} \cos \frac{\sqrt{3}q_y}{2} \right] \\ & + 2J_3 \left[\cos(2q_x) + 2 \cos q_x \cos(\sqrt{3}q_y) \right]. \end{aligned} \quad (11)$$

At the high-symmetry points

$$\Gamma = (0, 0), \quad K = \left(\frac{4\pi}{3}, 0 \right), \quad M = \left(\pi, \frac{\pi}{\sqrt{3}} \right) \quad (12)$$

the $\mathcal{J}_{\mathbf{q}}$ takes the following values:

$$\mathcal{J}_{\Gamma} = 6J_1 + 6J_2 + 6J_3, \quad (13a)$$

$$\mathcal{J}_K = -3J_1 + 6J_2 - 3J_3, \quad (13b)$$

$$\mathcal{J}_M = -2J_1 - 2J_2 + 6J_3. \quad (13c)$$

The ferromagnetic state corresponds to a minimum at Γ .

1. Stability of the ferromagnetic phase

The ferromagnetic state corresponds to a minimum at Γ . The direct crossings with the commensurate K occurs when $\mathcal{J}_K = \mathcal{J}_{\Gamma}$, which gives

$$J_1 + J_3 = 0. \quad (14)$$

Similarly, the crossing with the commensurate M -point minimum is determined by $\mathcal{J}_M = \mathcal{J}_{\Gamma}$, providing

$$J_1 + J_2 = 0 \quad (15)$$

On these two boundaries, the additional soft modes are located at the full symmetry stars of K and M , respectively.

There is also a long-wavelength instability of the ferromagnetic state. Expanding around Γ point in the Brillouin zone one finds

$$\mathcal{J}_{\mathbf{q}} - \mathcal{J}_{\Gamma} = -\frac{3}{2} (J_1 + 3J_2 + 4J_3) |\mathbf{q}|^2 + O(q^4). \quad (16)$$

Thus, the spin stiffness vanishes on the Lifshitz line

$$J_1 + 3J_2 + 4J_3 = 0. \quad (17)$$

The softening on this boundary occurs at Γ : more precisely, modes with $|\mathbf{q}| \rightarrow 0$ become soft.

For the J_1 - J_2 - J_3 three-shell triangular lattice model, these conditions give the full Luttinger–Tisza stability region of the ferromagnetic state,

$$J_1 + 3J_2 + 4J_3 \leq 0, \quad (18a)$$

$$J_1 + J_2 \leq 0, \quad (18b)$$

$$J_1 + J_3 \leq 0. \quad (18c)$$

For $J_1 = -1$, Eqs. (18) becomes

$$J_2 \leq 1, \quad J_3 \leq 1, \quad 3J_2 + 4J_3 \leq 1. \quad (19)$$

In the physically common case $J_2, J_3 > 0$, the ferromagnet first becomes unstable through the long-wavelength condition $3J_2 + 4J_3 = 1$, reproducing the limiting values $J_2/|J_1| = 1/3$ for the J_1 - J_2 model.

2. Commensurate and spiral phases

Away from the ferromagnetic region, the ordering wave vector is obtained by comparing the local minima of $\mathcal{J}_{\mathbf{q}}$. The minimum at the commensurate K -point realizes the usual three-sublattice order, while the minimum at the M point is either a stripy phase (single- \mathbf{q}) or a four-sublattice order (triple- \mathbf{q} structure).

But the minima can also occur along the high-symmetry lines. On the ΓM line, parametrized by

$$\mathbf{q} = \left(q, \frac{q}{\sqrt{3}} \right), \quad 0 \leq q \leq \pi, \quad (20)$$

the non-endpoint extremal point satisfies

$$\cos q_{\Gamma M} = -\frac{J_1 + J_2}{2J_2 + 4J_3}, \quad (21)$$

provided the right-hand side lies in $[-1, 1]$. This corresponds to

$$\mathcal{J}_{\Gamma M} = 6J_1 + 6J_2 + 6J_3 - \frac{(J_1 + 3J_2 + 4J_3)^2}{2J_2 + 4J_3}. \quad (22)$$

It is useful to treat the ΓK line and the adjacent KM edge in an extended-zone scheme, as illustrated in Fig. 2. We parametrize

$$\mathbf{q} = (q, 0), \quad 0 \leq q \leq 2\pi. \quad (23)$$

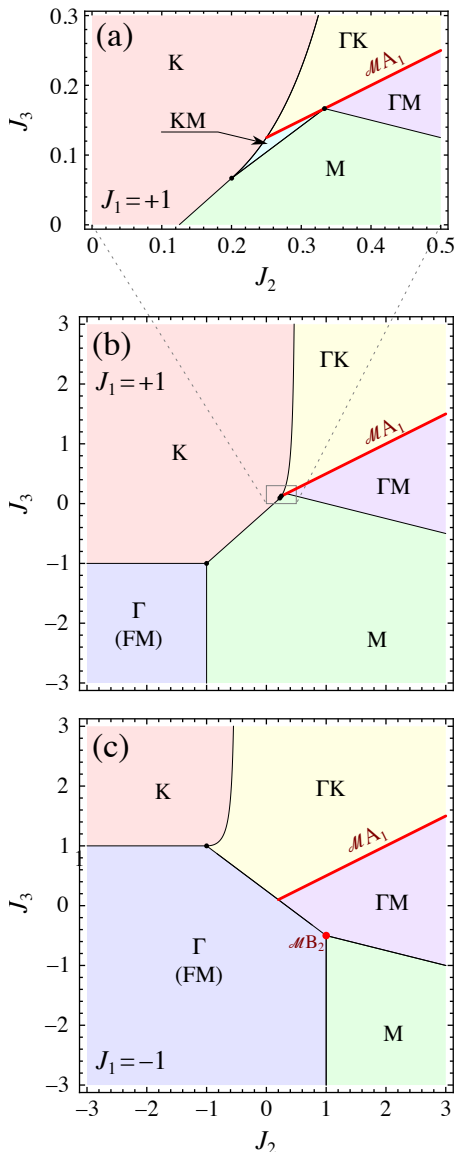


FIG. 3. Luttinger–Tisza phase diagram of the triangular-lattice J_1 - J_2 - J_3 Heisenberg model. Panels (a) and (b) show the antiferromagnetic nearest-neighbor case, $J_1 = +1$, with panel (a) giving an enlarged view of the central region of panel (b). Panel (c) shows the ferromagnetic nearest-neighbor case, $J_1 = -1$. Colors indicate the ordering wave vector \mathbf{q} at which $\mathcal{J}_{\mathbf{q}}$ is minimized. They distinguish the commensurate Γ , K , and M regions from incommensurate spiral regions whose minima lie on the high-symmetry lines ΓK , ΓM , and KM . Equivalently, these wave vectors are the momenta at which the single-magnon dispersion softens. The thick red line marks the $J_2 = 2J_3$ locus associated with the \mathcal{M}_{A_1} minimum manifold [Eq. (29)], while the red circle in panel (c) marks the fine-tuned point $(J_1, J_2, J_3) = (-1, 1, -1/2)$, where the \mathcal{M}_{B_2} nodal-line minimum manifold is realized [Eq. (34)].

This path starts at Γ , passes through K at $q = 4\pi/3$, and ends at a symmetry-equivalent M point at $q = 2\pi$. The

condition for the minimum (extremum) factorizes as

$$\frac{d\mathcal{J}_{(q,0)}}{dq} = -\sin\frac{q}{2} \left(1 + 2\cos\frac{q}{2}\right) \times \left[J_1 - 3J_2 + (6J_2 - 4J_3)\cos\frac{q}{2} + 8J_3\cos^2\frac{q}{2}\right] \quad (24)$$

The first factor gives the endpoints $q = 0$ and $q = 2\pi$, corresponding to Γ and M , respectively. The second factor gives the K point, $\cos(q/2) = -1/2$, i.e. $q = 4\pi/3$. The remaining minimal points are determined by

$$J_1 - 3J_2 + (6J_2 - 4J_3)\cos\frac{q}{2} + 8J_3\cos^2\frac{q}{2} = 0. \quad (25)$$

Thus, for $J_3 \neq 0$,

$$\cos\frac{q_{\pm}}{2} = \frac{2J_3 - 3J_2 \pm \sqrt{(3J_2 + 2J_3)^2 - 8J_1J_3}}{8J_3}. \quad (26)$$

The Luttinger–Tisza phase diagram is then obtained by keeping only those stationary points that are true minima and comparing their values of $\mathcal{J}_{\mathbf{q}}$. In Fig. 3, we show the ordering vectors separately for ferromagnetic ($J_1 = -1$) and antiferromagnetic ($J_1 = 1$) nearest-neighbor exchange.

3. Codimension-one minimum manifolds

An exact degeneracy occurs on the line $J_2 = 2J_3$ as a consequence of the relation between the triangular-lattice harmonics in Eqs. (A6),

$$2\gamma_{\mathbf{q}}^{(2)} + \gamma_{\mathbf{q}}^{(3)} = 6\left[\gamma_{\mathbf{q}}^{(1)}\right]^2 - 2\gamma_{\mathbf{q}}^{(1)} - 1. \quad (27)$$

Therefore, on $J_2 = 2J_3$,

$$\mathcal{J}_{\mathbf{q}} = 18J_2 \left[\gamma_{\mathbf{q}}^{(1)} + \frac{J_1 - J_2}{6J_2}\right]^2 - \frac{(J_1 - J_2)^2}{2J_2} - 3J_2. \quad (28)$$

For $J_2 > 0$, the coefficient of the square is positive. If the value required to make the square vanish lies within the range of the nearest-neighbor harmonic, the global minima form the contour

$$\mathcal{M}_{A_1} = \left\{ \mathbf{q} \in \text{BZ} \left| \gamma_{\mathbf{q}}^{(1)} = \frac{J_2 - J_1}{6J_2} \right. \right\}. \quad (29)$$

Here the subscript indicates that the manifold is defined as a level set of the fully symmetric A_1 harmonic $\gamma_{\mathbf{q}}^{(1)}$. Since $-1/2 \leq \gamma_{\mathbf{q}}^{(1)} \leq 1$, the contour exists when

$$-\frac{1}{2} \leq \frac{J_2 - J_1}{6J_2} \leq 1. \quad (30)$$

For $J_1 > 0$, this is the spiral-spin-liquid line discussed in Ref. [51]. For $J_1 < 0$, the same square completion gives the corresponding ferromagnetic-side spiral contour once the Γ minimum becomes unstable. For example, with

$J_1 = -1$ and $J_2 = 2J_3 > 0$, the contour emerges from the Γ point at $J_2 = 1/5$, where the condition in Eq. (30) is first satisfied. This coincides with the Lifshitz boundary in Eq. (17); for $J_2 > 1/5$, the degenerate manifold is a finite contour around Γ .

The square-completion form in Eq. (28) shows that the line $J_2 = 2J_3$ is a simple triangular-lattice realization of the general codimension-one spiral-manifold construction for Bravais-lattice Heisenberg models [54]. In the present two-dimensional case, the Luttinger–Tisza minima are determined by a single scalar constraint on \mathbf{q} , and therefore form a one-dimensional contour in the Brillouin zone.

A second exact codimension-one minimum manifold occurs at the fine-tuned point $(J_1, J_2, J_3) = (-1, 1, -1/2)$. This degeneracy is naturally expressed in terms of a one-dimensional nontrivial lattice harmonic. With the bond convention of Appendix A, define

$$\beta_{\mathbf{q}}^{(1)} = \frac{1}{3} \left[\sin(\mathbf{q} \cdot \boldsymbol{\delta}_1^{(1)}) - \sin(\mathbf{q} \cdot \boldsymbol{\delta}_2^{(1)}) + \sin(\mathbf{q} \cdot \boldsymbol{\delta}_3^{(1)}) \right]. \quad (31)$$

Equivalently,

$$\beta_{\mathbf{q}}^{(1)} = \frac{2}{3} \sin \frac{q_x}{2} \left[\cos \frac{q_x}{2} - \cos \frac{\sqrt{3}q_y}{2} \right]. \quad (32)$$

This harmonic transforms according to the \mathbf{B}_2 irreducible representation of D_6 . At the special point, the exchange Fourier transform takes the exact square form

$$\mathcal{J}_{\mathbf{q}} = -3 + 18 \left[\beta_{\mathbf{q}}^{(1)} \right]^2. \quad (33)$$

Hence the Luttinger–Tisza minima are given by the nodal manifold

$$\mathcal{M}_{\mathbf{B}_2} = \left\{ \mathbf{q} \in \text{BZ} \mid \beta_{\mathbf{q}}^{(1)} = 0 \right\}, \quad (34)$$

or explicitly,

$$\sin \frac{q_x}{2} = 0 \quad \text{or} \quad \cos \frac{q_x}{2} - \cos \frac{\sqrt{3}q_y}{2} = 0. \quad (35)$$

Thus $\mathcal{M}_{\mathbf{B}_2}$ is a union of symmetry-related lines in the Brillouin zone. This fine-tuned point therefore gives a second triangular-lattice realization of a codimension-one minimum manifold in the sense of Ref. [54], distinct from the $J_2 = 2J_3$ line where the square completion involves the fully symmetric A_1 harmonic $\gamma_{\mathbf{q}}^{(1)}$.

In Fig. 3, the parameter-space loci associated with these two manifolds are indicated: the $J_2 = 2J_3$ line giving $\mathcal{M}_{\mathbf{A}_1}$ is shown by a red line, while the fine-tuned point $(J_2, J_3) = (1, -1/2)$ giving $\mathcal{M}_{\mathbf{B}_2}$ for $J_1 = -1$ is marked by a red circle.

IV. ONE-MAGNON SECTOR

Here we revisit the same exchange Fourier transform from the viewpoint needed for the high-field problem: we

identify the ferromagnetic stability boundaries and relate the Luttinger–Tisza minima directly to the one-magnon dispersion above the fully polarized state.

A. Heisenberg interactions

Let us denote the fully polarized state by $|\text{FM}\rangle$. For the Heisenberg model (3), its energy is

$$E_0 = \langle \text{FM} | \hat{H}_{\text{Heis}} | \text{FM} \rangle = \frac{1}{2} N S^2 \mathcal{J}_0. \quad (36)$$

A normalized one-magnon Bloch state is

$$|\psi_{\mathbf{q}}^{(1)}\rangle = \frac{1}{\sqrt{2SN}} \sum_j e^{-i\mathbf{q} \cdot \mathbf{r}_j} \hat{S}_j^- | \text{FM} \rangle. \quad (37)$$

Direct evaluation gives

$$\varepsilon_{\mathbf{q}} = E_{\mathbf{q}} - E_0 = S(\mathcal{J}_{\mathbf{q}} - \mathcal{J}_0). \quad (38)$$

Thus, the one-magnon soft modes are precisely the Luttinger–Tisza minima of $\mathcal{J}_{\mathbf{q}}$, measured relative to the ferromagnetic point Γ .

At the commensurate points,

$$\varepsilon_K = -9S(J_1 + J_3), \quad (39)$$

$$\varepsilon_M = -8S(J_1 + J_2), \quad (40)$$

whereas near Γ ,

$$\varepsilon_{\mathbf{q}} = -\frac{3S}{2} (J_1 + 3J_2 + 4J_3) |\mathbf{q}|^2 + O(q^4). \quad (41)$$

the analog of Eq. (16). The single-magnon stability of the fully polarized state at zero field is therefore equivalent to the Luttinger–Tisza stability condition in Eq. (18). In a magnetic field, a one-magnon state has $S_{\text{tot}}^z = NS - 1$ and therefore costs an additional Zeeman energy h , Eq. (9). The one-magnon dispersion becomes

$$\varepsilon_{\mathbf{q}}(h) = h + S(\mathcal{J}_{\mathbf{q}} - \mathcal{J}_0). \quad (42)$$

It follows that the one-magnon saturation field is

$$h_s^{(1)} = S \left[\mathcal{J}_0 - \min_{\mathbf{q}} \mathcal{J}_{\mathbf{q}} \right]. \quad (43)$$

If the leading instability of the saturated state is in the one-magnon channel, magnons condense at the minimizing wave vector below $h_s^{(1)}$, producing the corresponding transverse magnetic order [4]. The two-magnon calculation below asks whether a bound state softens at a higher field than this single-magnon instability.

B. Scalar spin chirality

The scalar-chirality interaction is qualitatively different from the Heisenberg exchange terms because it is

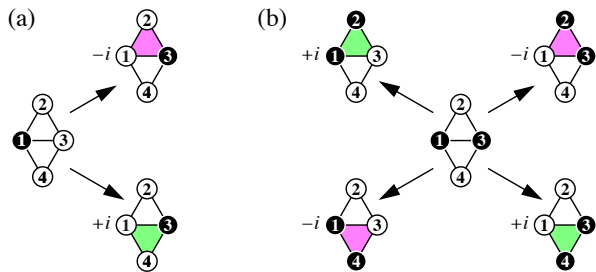


FIG. 4. Action of the uniform scalar spin chirality interaction $4(\hat{\chi}_{123} + \hat{\chi}_{134}) = i\hat{P}_{123} - i\hat{P}_{132} + i\hat{P}_{134} - i\hat{P}_{143}$ for spin-1/2 one- and two-magnon states; see Eq. (7). Empty circles denote up spins and filled circles down spins. Colored triangles indicate the permutation terms that act nontrivially on the displayed spin configuration; the color encodes the sign of the imaginary amplitude, with magenta denoting $-i$ and green $+i$. (a) In the one-magnon sector, the down spin on site 1 can hop to site 3 through two oriented triangles, corresponding to the processes $-i\hat{P}_{132}$ and $+i\hat{P}_{134}$. These two amplitudes cancel, so the scalar-chirality term does not contribute to the one-magnon dispersion. (b) In the two-magnon sector, a neighboring down spin leaves uncompensated oriented imaginary amplitudes. These amplitudes originate from the time-reversal-odd scalar-chirality operator and act as a chiral interaction between magnons.

trilinear in spin operators. This prevents us from incorporating it by a simple modification of the Fourier-transformed exchange $\mathcal{J}_{\mathbf{q}}$ into the Luttinger–Tisza analysis. Instead, we evaluate its action directly in the one- and two-magnon sectors above the fully polarized state.

For spin 1/2, Eq. (7) expresses the scalar chirality on an oriented triangle in terms of cyclic permutations. This representation makes the cancellation in the one-magnon sector transparent. For the uniform chirality pattern considered here, a single flipped spin can hop through the two oriented triangles sharing a bond, but the two amplitudes have opposite signs. As illustrated in Fig. 4, the processes $-i\hat{P}_{132}$ and $+i\hat{P}_{134}$ both move the down spin from site (1) to site (3), and their amplitudes cancel. Thus the scalar-chirality term has no matrix elements within the one-magnon subspace,

$$\langle \psi_{\mathbf{q}}^{(1)} | \hat{H}_{\text{Chir}} | \psi_{\mathbf{q}}^{(1)} \rangle = 0, \quad (44)$$

and the scalar-chirality term does not contribute to the one-magnon dispersion (it also leaves the ferromagnetic energy intact). The single-magnon spectrum is therefore still given by Eq. (38).

Thus, the scalar-chirality term leaves the one-magnon problem unchanged: the one-magnon saturation field and the soft-mode wave vectors are still determined by the Heisenberg dispersion $\varepsilon_{\mathbf{q}}$. This statement is restricted to the magnon spectrum above the fully polarized state, and does not amount to a Luttinger–Tisza treatment of the full Hamiltonian.

The two-magnon sector is different. When two neighboring spins are flipped, the local pairwise cancellation present for an isolated magnon is incomplete. The scalar-

chirality term then produces uncompensated oriented imaginary amplitudes, which enter the two-magnon problem as an interaction vertex rather than as a correction to the one-magnon kinetic energy. Since the scalar chirality is odd under time reversal, this interaction distinguishes opposite senses of relative motion of the two magnons. We derive its explicit contribution to the two-magnon Schrödinger equation below.

This mechanism is closely related to the kinetic origin of magnon pairing in frustrated ferromagnets with cyclic exchange, where neighboring flipped spins can propagate coherently even when the one-magnon motion is strongly suppressed [55]. In the present case, however, the corresponding pair motion is generated by the time-reversal-odd combination $i\hat{P} - i\hat{P}^{-1}$. The scalar-chirality term therefore produces a chiral analog of magnon-pair hopping: it leaves the one-magnon dispersion unchanged, but contributes finite oriented amplitudes in the two-magnon sector.

V. TWO-MAGNON SECTOR

We now turn to the two-magnon problem above the fully polarized state, restricting throughout to spin 1/2. This is the minimal sector in which magnon interactions appear. The problem of two-spin-wave bound states in ferromagnets has a long history [56–58]. In frustrated ferromagnets, such bound states can soften before the one-magnon mode and drive multipolar, in particular spin-nematic, instabilities [3, 8, 10, 12, 41, 59].

Our derivation follows Ref. [8, 12], adapted here to the $S = 1/2$ triangular-lattice J_1 - J_2 - J_3 model, including the scalar-chirality interaction. We first write the two-magnon Schrödinger equation in momentum space, where the one-magnon hopping determines the kinetic part and the interaction enters through a two-particle scattering kernel. We then express this kernel in a finite basis of lattice harmonics, or partial-wave channels, appropriate to the finite range of the interactions. This partial-wave representation reduces the two-magnon bound-state problem to a finite-dimensional eigenvalue equation.

A. Two-magnon Schrödinger equation for the Heisenberg terms

We work in the spin-1/2 two-magnon Hilbert space above the fully polarized state. A configuration-space basis state is

$$|i, j\rangle = \hat{S}_j^- \hat{S}_i^- |\text{FM}\rangle, \quad i \neq j, \quad (45)$$

where the condition $i \neq j$ enforces the hard-core constraint for spin 1/2. We introduce the two-magnon momentum states

$$|\mathbf{k}, \mathbf{k}'\rangle_{\text{R}} = \frac{1}{2N} \sum_{i \neq j} e^{-i\mathbf{k}\cdot\mathbf{r}_i} e^{-i\mathbf{k}'\cdot\mathbf{r}_j} |i, j\rangle, \quad (46)$$

where the subscript R stands for the ‘regular’ states respecting the hard-core constraint. In terms of the total momentum

$$\mathbf{K} = \mathbf{k} + \mathbf{k}' \quad (47)$$

and relative momentum

$$\mathbf{q} = \frac{\mathbf{k}' - \mathbf{k}}{2}, \quad (48)$$

this state becomes

$$|\mathbf{K}, \mathbf{q}\rangle_{\text{R}} = \frac{1}{2N} \sum_{i \neq j} e^{-i\frac{\mathbf{K}}{2} \cdot (\mathbf{r}_i + \mathbf{r}_j)} e^{-i\mathbf{q} \cdot (\mathbf{r}_j - \mathbf{r}_i)} |i, j\rangle. \quad (49)$$

Since the two flipped spins are indistinguishable,

$$|\mathbf{K}, \mathbf{q}\rangle_{\text{R}} = |\mathbf{K}, -\mathbf{q}\rangle_{\text{R}}, \quad (50)$$

the wave function describing the two flipped $S = 1/2$ is even under $\mathbf{q} \rightarrow -\mathbf{q}$.

A general two-magnon wave function at fixed total momentum \mathbf{K} is then written as

$$|\Psi_{\mathbf{K}}\rangle = \sum_{\mathbf{q}} \psi_{\mathbf{K}}^{\text{R}}(\mathbf{q}) |\mathbf{K}, \mathbf{q}\rangle_{\text{R}}. \quad (51)$$

The Schrödinger equation for the momentum-space wave function is

$$\left(E_2 - \varepsilon_{\frac{\mathbf{K}}{2} - \mathbf{q}} - \varepsilon_{\frac{\mathbf{K}}{2} + \mathbf{q}} \right) \psi_{\mathbf{K}}^{\text{R}}(\mathbf{q}) = \frac{1}{N} \sum_{\mathbf{p}} V_{\mathbf{K}}(\mathbf{q}, \mathbf{p}) \psi_{\mathbf{K}}^{\text{R}}(\mathbf{p}), \quad (52)$$

with interaction kernel

$$V_{\mathbf{K}}(\mathbf{q}, \mathbf{p}) = \frac{1}{2} \left(\mathcal{J}_{\mathbf{q} - \mathbf{p}} + \mathcal{J}_{\mathbf{q} + \mathbf{p}} - \mathcal{J}_{\frac{\mathbf{K}}{2} - \mathbf{p}} - \mathcal{J}_{\frac{\mathbf{K}}{2} + \mathbf{p}} \right) \quad (53)$$

$$= \varepsilon_{\mathbf{q} - \mathbf{p}} + \varepsilon_{\mathbf{q} + \mathbf{p}} - \varepsilon_{\frac{\mathbf{K}}{2} - \mathbf{p}} - \varepsilon_{\frac{\mathbf{K}}{2} + \mathbf{p}}. \quad (54)$$

Let us note that this kernel is the transpose of the more common convention in which the hard-core terms depend on \mathbf{q} rather than on \mathbf{p} [8, 12]. The two conventions give the same bound-state energies.

Using the lattice harmonics defined in Appendix A and the decomposition (A12), the kernel is separable as

$$V_{\mathbf{K}}^{(\text{H})}(\mathbf{q}, \mathbf{p}) = \sum_{\mu} V_{\mu} \tilde{\gamma}_{\mathbf{p}}^{\mu} R_{\mu}(\mathbf{q}, \frac{\mathbf{K}}{2}), \quad (55)$$

with

$$R_{\mu}(\mathbf{q}, \frac{\mathbf{K}}{2}) = \gamma_{\mathbf{q}}^{\mu} - \gamma_{\frac{\mathbf{K}}{2}}^{\mu}, \quad (56)$$

and

$$V_{\mu} = \begin{cases} 6J_n, & \mu = (n), \\ \frac{3}{2}J_n, & \mu = (n+), \\ \frac{3}{2}J_n, & \mu = (n-), \end{cases} \quad n = 1, 2, 3. \quad (57)$$

Here

$$\mu = \{(1), (2), (3), (1+), (2+), (3+), (1-), (2-), (3-)\} \quad (58)$$

enumerates the lattice harmonics defined in Eq. (A10). This form is the triangular-lattice analog of the partial-wave decomposition in the square-lattice problem [8, 12].

B. Effect of the scalar-chirality term

We now include the scalar-chirality interaction in the two-magnon problem. As shown in Sec. IV B, \hat{H}_{Chir} has no matrix elements within the one-magnon subspace and therefore does not modify the one-magnon dispersion $\varepsilon_{\mathbf{q}}$. Its first nontrivial effect appears in the two-magnon sector, where it contributes to the interaction kernel $V_{\mathbf{K}}(\mathbf{q}, \mathbf{p})$.

A convenient way to derive this contribution is to temporarily enlarge the two-magnon Hilbert space by adding auxiliary states having two spin flips on the same site (i.e., double occupancy states),

$$\mathcal{H}_{2\text{D}} = \{|j, j\rangle, j = 1, \dots, N\}, \quad (59)$$

so the enlarged Hilbert space is

$$\mathcal{H}_{2\text{X}} = \mathcal{H}_{2\text{R}} \oplus \mathcal{H}_{2\text{D}}, \quad (60)$$

where $\mathcal{H}_{2\text{R}}$ is the physical spin-1/2 two-magnon subspace introduced in Eq. (45), with the hard core $i \neq j$ constraint. The double-occupancy state at total momentum \mathbf{K} is

$$|\mathbf{K}\rangle_{\text{D}} = \sum_{j=1}^N e^{-i\mathbf{K} \cdot \mathbf{r}_j} |j, j\rangle. \quad (61)$$

The enlarged state is therefore

$$|\mathbf{K}, \mathbf{q}\rangle_{\text{X}} = |\mathbf{K}, \mathbf{q}\rangle_{\text{R}} \oplus |\mathbf{K}\rangle_{\text{D}}. \quad (62)$$

The double-occupancy is only for bookkeeping purposes, and at the end of the calculation, we project back to the physical subspace with

$$\hat{\mathcal{P}}_{2\text{R}} = \hat{\mathbf{1}}_{2\text{X}} - \sum_{j=1}^N |j, j\rangle \langle j, j|. \quad (63)$$

The role of the auxiliary sector is to separate the free two-magnon propagation from the genuine interaction terms. We define \hat{H}_0 in the enlarged space by its action on the momentum states,

$$\hat{H}_0 |\mathbf{K}, \mathbf{q}\rangle_{\text{X}} = \left(\varepsilon_{\frac{\mathbf{K}}{2} + \mathbf{q}} + \varepsilon_{\frac{\mathbf{K}}{2} - \mathbf{q}} \right) |\mathbf{K}, \mathbf{q}\rangle_{\text{X}}. \quad (64)$$

The interaction is then the projected difference between the full Hamiltonian and this free propagation,

$$\hat{V} = \hat{\mathcal{P}}_{2\text{R}} \left(\hat{H} - \hat{H}_0 \right) \hat{\mathcal{P}}_{2\text{R}}. \quad (65)$$

For the Heisenberg terms this construction reproduces Eq. (54). For the scalar-chirality term it gives the additional contribution

$$V_{\mathbf{K}}^{(\text{X})}(\mathbf{q}, \mathbf{p}) = -i 12\sqrt{3}J_{\chi} \left[\gamma_{\mathbf{p}}^{(1)} \left(\gamma_{\frac{\mathbf{K}}{2}}^{(1a)} \gamma_{\mathbf{q}}^{(1b)} - \gamma_{\frac{\mathbf{K}}{2}}^{(1b)} \gamma_{\mathbf{q}}^{(1a)} \right) + \gamma_{\mathbf{p}}^{(1a)} \left(\gamma_{\frac{\mathbf{K}}{2}}^{(1b)} \gamma_{\mathbf{q}}^{(1)} - \gamma_{\frac{\mathbf{K}}{2}}^{(1)} \gamma_{\mathbf{q}}^{(1b)} \right) + \gamma_{\mathbf{p}}^{(1b)} \left(\gamma_{\frac{\mathbf{K}}{2}}^{(1)} \gamma_{\mathbf{q}}^{(1a)} - \gamma_{\frac{\mathbf{K}}{2}}^{(1a)} \gamma_{\mathbf{q}}^{(1)} \right) \right]. \quad (66)$$

Equivalently, in the complex C_6 harmonics this can be written as

$$V_{\mathbf{K}}^{(\chi)}(\mathbf{q}, \mathbf{p}) = -6\sqrt{3}J_\chi \left[\gamma_{\frac{\mathbf{K}}{2}}^{(1)} \left(\bar{\gamma}_{\mathbf{p}}^{(1-)} \gamma_{\mathbf{q}}^{(1-)} - \bar{\gamma}_{\mathbf{p}}^{(1+)} \gamma_{\mathbf{q}}^{(1+)} \right) + \gamma_{\frac{\mathbf{K}}{2}}^{(1+)} \left(\bar{\gamma}_{\mathbf{p}}^{(1+)} \gamma_{\mathbf{q}}^{(1)} - \bar{\gamma}_{\mathbf{p}}^{(1-)} \gamma_{\mathbf{q}}^{(1-)} \right) + \gamma_{\frac{\mathbf{K}}{2}}^{(1-)} \left(\bar{\gamma}_{\mathbf{p}}^{(1)} \gamma_{\mathbf{q}}^{(1+)} - \bar{\gamma}_{\mathbf{p}}^{(1-)} \gamma_{\mathbf{q}}^{(1)} \right) \right]. \quad (67)$$

This form makes it explicit that the scalar-chirality term, linear in J_χ , splits the states that transform under the two-dimensional irreducible representation E_2 . enters as a separable chiral contribution to the two-magnon interaction matrix. Under time reversal, complex conjugation compensates for the change of the sign of the J_χ . The full interaction kernel used below is therefore

$$V_{\mathbf{K}}(\mathbf{q}, \mathbf{p}) = V_{\mathbf{K}}^{(H)}(\mathbf{q}, \mathbf{p}) + V_{\mathbf{K}}^{(\chi)}(\mathbf{q}, \mathbf{p}), \quad (68)$$

where $V_{\mathbf{K}}^{(H)}$ is the Heisenberg kernel in Eq. (54).

C. Gap equation for the bound-state criterion

1. Binding energy

A bound state at fixed total momentum \mathbf{K} occurs when its energy E_2 lies below the lower edge of the two-magnon continuum,

$$E_{\text{cont}}^{\min}(\mathbf{K}) = \min_{\mathbf{q}} \left[\varepsilon_{\frac{\mathbf{K}}{2} + \mathbf{q}} + \varepsilon_{\frac{\mathbf{K}}{2} - \mathbf{q}} \right]. \quad (69)$$

We parameterize the bound-state energy as

$$E_2 = E_{\text{cont}}^{\min}(\mathbf{K}) - \Delta, \quad \Delta > 0. \quad (70)$$

Equivalently, if \mathbf{q}_{\min} minimizes the continuum energy at fixed \mathbf{K} , then

$$E_2 = \varepsilon_{\frac{\mathbf{K}}{2} + \mathbf{q}_{\min}} + \varepsilon_{\frac{\mathbf{K}}{2} - \mathbf{q}_{\min}} - \Delta. \quad (71)$$

Beyond the ferromagnetic phase, the binding energy determines the instability of the fully polarized state as the magnetic field decreases. Since an n -magnon state lowers the total S^z by n , the Zeeman term of the form given in Eq. (9) lowers its energy E_n to

$$E_n(h) = E_n - nh. \quad (72)$$

As a consequence, the n -magnon instability occurs at a field for which $E_n(h)$ is below the energy E_0 of the ferromagnetic state: $E_0 > E_n(h)$, i.e., at a field

$$h_c^{(n)} = \frac{1}{n}(E_n - E_0) \quad (73)$$

and the actual saturation field is the maximum value of $h_c^{(n)}$, $n = 1, 2, 3, \dots$, into a state having n magnons. The one-magnon instability occurs at

$$h_c^{(1)} = -\min_{\mathbf{q}} \varepsilon_{\mathbf{q}}, \quad (74)$$

whereas a two-magnon instability

$$h_c^{(2)}(\mathbf{K}) = \frac{1}{2}(E_{\text{cont}}^{\min}(\mathbf{K}) - \Delta), \quad (75)$$

Since typically the continuum minimum arises by two magnons at the one-magnon minimum, $E_{\text{cont}}^{\min} = 2\varepsilon_{\min}$, (though we need to be careful that two distinct momenta can occupy ε_{\min}), the

$$h_c^{(2)} = h_c^{(1)} + \frac{\Delta}{2}. \quad (76)$$

and a finite gap increases the saturation field. In this situation, as the field lowers, the two-magnon bound state condenses before the single-magnon gap closes, leaving the one-magnon excitations gapped at the transition. The resulting phase just below saturation is then a spin-nematic phase, supposing that the binding energy of three or more magnons allows it.

2. Gap equation

Below, we concentrate on the $\mathbf{K} = \Gamma$ total momentum. In the ferromagnetic region, the lowest two-magnon continuum occurs at $\mathbf{K} = \Gamma$. It is then plausible that the bound states relevant to the instability of the fully polarized state are found at the same total momentum. We therefore set $\mathbf{K} = 0$ from this point on. We assume this also holds in other parts of the phase diagram.

For $\mathbf{K} = 0$, the scalar-chirality contribution reduces to a shift of the first-neighbor chiral channels,

$$V_{1+} = \frac{3}{2}J_1 + 6\sqrt{3}J_\chi, \quad (77a)$$

$$V_{1-} = \frac{3}{2}J_1 - 6\sqrt{3}J_\chi, \quad (77b)$$

leaving the A_1 channel intact. Substituting the kernel

$$V_{\mathbf{K}=0}(\mathbf{q}, \mathbf{p}) = \sum_{\mu} V_{\mu} \bar{\gamma}_{\mathbf{p}}^{\mu} R_{\mu}(\mathbf{q}, 0) \quad (78)$$

with

$$R_{\mu}(\mathbf{q}, 0) = \gamma_{\mathbf{q}}^{\mu} - \gamma_{\mathbf{0}}^{\mu} \quad (79)$$

into the Schrödinger Eq. (52) gives

$$(E_2 - 2\varepsilon_{\mathbf{q}}) \psi_0^{\text{R}}(\mathbf{q}) = \frac{1}{N} \sum_{\mathbf{p}, \mu} V_{\mu} R_{\mu}(\mathbf{q}, 0) \bar{\gamma}_{\mathbf{p}}^{\mu} \psi_0^{\text{R}}(\mathbf{p}). \quad (80)$$

We now introduce the partial-wave amplitudes

$$S_{\mu} = \frac{1}{N} \sum_{\mathbf{p}} \bar{\gamma}_{\mathbf{p}}^{\mu} \psi_0^{\text{R}}(\mathbf{p}). \quad (81)$$

Then Eq. (80) can be written as

$$\psi_0^{\text{R}}(\mathbf{q}) = \sum_{\mu} \frac{V_{\mu} R_{\mu}(\mathbf{q}, 0)}{E_2 - 2\varepsilon_{\mathbf{q}}} S_{\mu}. \quad (82)$$

Substituting this expression back into Eq. (81) gives a closed self-consistency equation for the partial-wave amplitudes in the form of a homogeneous linear system,

$$S_\nu = \sum_\mu \mathcal{I}_{\nu\mu}(E_2) S_\mu, \quad (83)$$

where

$$\mathcal{I}_{\nu\mu}(E_2) = \frac{1}{N} \sum_{\mathbf{p}} \frac{V_\mu \tilde{\gamma}_{\mathbf{p}}^\nu R_\mu(\mathbf{p}, 0)}{E_2 - 2\varepsilon_{\mathbf{p}}}. \quad (84)$$

A nontrivial solution exists when

$$\det[\mathcal{I}(E_2) - \mathbf{1}] = 0. \quad (85)$$

This is the gap equation for the two-magnon bound state.

At $\mathbf{K} = 0$, symmetry block diagonalizes Eq. (83) into three independent 3×3 matrices. The matrix in the A_1 symmetric channel is

$$\begin{pmatrix} \mathcal{I}_{1,1} & \mathcal{I}_{1,2} & \mathcal{I}_{1,3} \\ \mathcal{I}_{2,1} & \mathcal{I}_{2,2} & \mathcal{I}_{2,3} \\ \mathcal{I}_{3,1} & \mathcal{I}_{3,2} & \mathcal{I}_{3,3} \end{pmatrix}, \quad (86a)$$

with matrix elements

$$\mathcal{I}_{n,m} = \frac{1}{N} \sum_{\mathbf{p}} \frac{V_m \tilde{\gamma}_{\mathbf{p}}^{(n)} [\gamma_{\mathbf{p}}^{(m)} - 1]}{E_2 - 2\varepsilon_{\mathbf{p}}}. \quad (86b)$$

and couplings

$$(V_1, V_2, V_3) = (6J_1, 6J_2, 6J_3). \quad (86c)$$

The 3×3 matrix in the $+$ chiral channel is

$$\begin{pmatrix} \mathcal{I}_{1+,1+} & \mathcal{I}_{1+,2+} & \mathcal{I}_{1+,3+} \\ \mathcal{I}_{2+,1+} & \mathcal{I}_{2+,2+} & \mathcal{I}_{2+,3+} \\ \mathcal{I}_{3+,1+} & \mathcal{I}_{3+,2+} & \mathcal{I}_{3+,3+} \end{pmatrix}; \quad (87a)$$

for the $-$ channel we replace $+$ $\rightarrow -$ in labels. The matrix elements are

$$\mathcal{I}_{n\pm, m\pm}(E_2) = \frac{1}{N} \sum_{\mathbf{p}} \frac{V_{m\pm} \tilde{\gamma}_{\mathbf{p}}^{(n\pm)} \gamma_{\mathbf{p}}^{(m\pm)}}{E_2 - 2\varepsilon_{\mathbf{p}}} \quad (87b)$$

and the couplings are

$$V_{1\pm} = \frac{3}{2} J_1 \pm 6\sqrt{3} J_\chi, \quad (87c)$$

$$V_{2\pm} = \frac{3}{2} J_2, \quad (87d)$$

$$V_{3\pm} = \frac{3}{2} J_2. \quad (87e)$$

Thus, the scalar-chirality interaction splits the $+$ and $-$ partial-wave sectors by shifting the first-neighbor coupling in opposite directions, thereby manifesting the time-reversal-odd character of the scalar chirality.

To locate the instability of the fully polarized state, we set $E_2 = 0$ in the secular equation. At $J_\chi = 0$, the zero contour of

$$\det[\mathcal{I}(E_2 = 0) - \mathbf{1}] = 0 \quad (88)$$

gives the boundary where the two-magnon bound state first softens. For $J_\chi \neq 0$, the one-magnon dispersion, and hence the denominator in Eq. (84), is unchanged. Since the scalar chirality only shifts the first-neighbor couplings in the chiral sectors, Eq. (87c), the J_χ appears only in the first column of the matrix $\mathcal{I} - \mathbf{1}$ in each of the $+$ and $-$ blocks, Eq. (87a). Since the determinant is linear in each column separately, the secular equation is linear in J_χ for fixed J_1, J_2, J_3 . Solving this equation gives the value of J_χ for which the two-magnon bound state at $\mathbf{K} = 0$ becomes gapless.

The same secular equation can also be used to determine where a bound state first separates from the two-magnon continuum at a finite field. In this case, one sets

$$E_2 = E_{\text{cont}}^{\min}(\mathbf{K}), \quad (89)$$

rather than $E_2 = 0$. For $\mathbf{K} = 0$ we considered here, this gives

$$E_2 = E_{\text{cont}}^{\min}(0) = \min_{\mathbf{q}} 2\varepsilon_{\mathbf{q}}. \quad (90)$$

This criterion locates the point where the two-magnon bound-state branch detaches from the continuum.

VI. RESULTS

We now apply the two-magnon formulation derived above to the triangular-lattice J_1 - J_2 - J_3 model. We use two complementary diagnostics. First, we perform exact diagonalization in the two-magnon sector on periodic clusters with full sixfold lattice symmetry. This gives the full momentum-resolved two-magnon spectrum and allows us to identify bound states at arbitrary total momentum. Second, we use the separable partial-wave gap equation at $\mathbf{K} = 0$, Eq. (85), to resolve the dominant symmetry channels and to study the effect of the scalar chirality term.

Figure 5 shows representative exact diagonalization spectra for an $N = 3 \times 24^2 = 1728$ cluster. The grey region denotes the two-magnon continuum, while the isolated red levels below it are bound states. The examples illustrate three important points. First, bound states are strongly enhanced near parameter values where the one-magnon dispersion has an anomalously degenerate set of minima. This is most clearly seen at $(J_1, J_2, J_3) = (-1, 1, -1/2)$, where the \mathcal{M}_{B_2} nodal-line minimum manifold produces an extended flat lower edge of the two-magnon continuum. At this point the lowest bound state belongs to the twofold E_2 -type channel and has a large binding energy, as also shown in Table I. Second, ordinary long-wavelength softening at the Lifshitz boundary

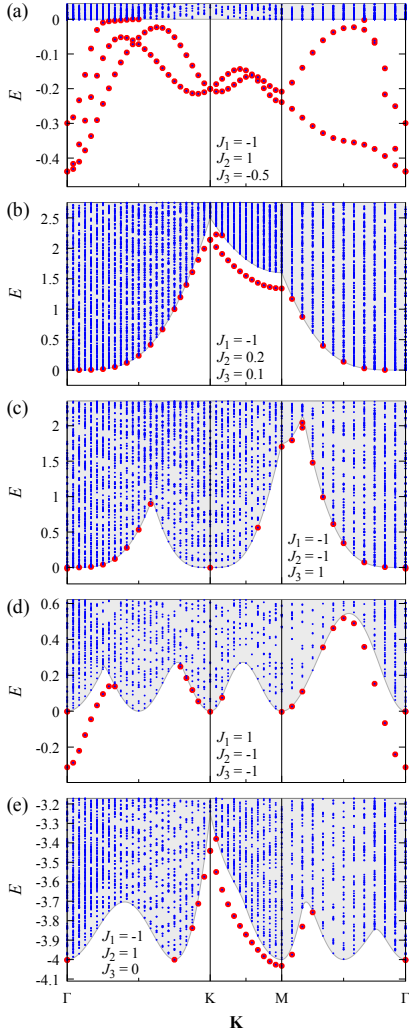


FIG. 5. Exact-diagonalization spectra in the two-magnon sector for an $N = 3 \times 24^2 = 1728$ cluster at selected values of (J_1, J_2, J_3) . The total momentum \mathbf{K} is along the Γ - K - M - Γ path in the Brillouin zone. The gray shaded regions indicate the two-magnon continuum, blue points show the finite-size two-magnon energies, and red circles mark levels lying below the lower continuum edge. (a) Spectrum at the fine-tuned point where the \mathcal{M}_{B_2} nodal-line minimum manifold is realized. The flat lower continuum edge reflects the dispersionless one-magnon minima along high-symmetry lines. (b) Spectrum at the point where the Lifshitz boundary meets the \mathcal{M}_{A_1} manifold; no bound state is found below the continuum. (c) Spectrum at a point where the ferromagnetic phase boundary meets the K and ΓK regions. (d) Example with the largest binding energy found in the scanned antiferromagnetic- J_1 parameter regime. A well-developed bound state appears at the Γ point in the A_1 channel. (e) Example in which the lowest bound state occurs at the M point rather than at Γ .

is not by itself sufficient to guarantee a bound state: for $(J_1, J_2, J_3) = (-1, 1/5, 1/10)$ — where the \mathcal{M}_{A_1} manifold meets the Lifshitz boundary — the finite-size spectrum shows no bound state below the 2-magnon continuum at

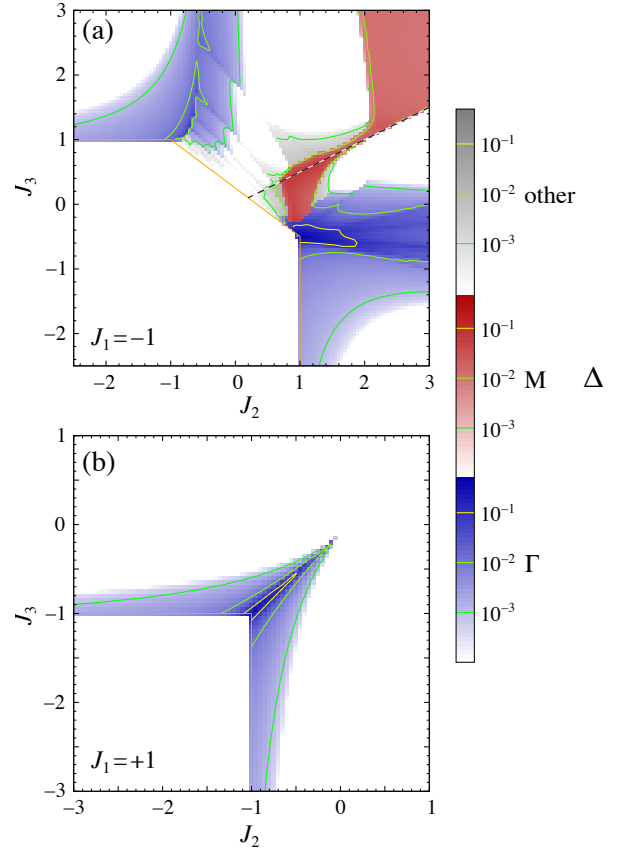


FIG. 6. Scan of the momentum and the gap of the lowest energy bound state in the J_2 - J_3 parameter space for (a) ferromagnetic and (b) antiferromagnetic J_1 exchanges. We use Eq. (70) to calculate the gap Δ with energies from an exact diagonalization calculation of a $3 \times 24^2 = 1728$ -site cluster. The lowest energy bound state is mostly at the $\mathbf{K} = \Gamma$ point, while there are some regions where it is at the M point, and at incommensurate values where the minima of the single magnon dispersion are also incommensurate, in the ΓK or ΓM phase. The largest value of the gap is at $(J_1, J_2, J_3) = (-1, 1, -1/2)$ and $(1, -1, -1)$. The thin orange lines denote the boundary of the ferromagnetic phase, and the dashed black and white line the \mathcal{M}_{A_1} manifold.

the current resolution. Third, although the lowest bound states often occur at total momentum $\mathbf{K} = \Gamma$, this is not universal. For example, at $(J_1, J_2, J_3) = (-1, 1, 0)$, the dominant bound state occurs at the M point, with a binding energy substantially larger than that of the corresponding Γ -point level. The lower boundary of the M region roughly follows the line of the \mathcal{M}_{A_1} manifold.

The momentum-resolved scan in Fig. 6 summarizes this behavior over the J_2 - J_3 plane for both signs of J_1 . For each parameter point we identify the lowest two-magnon level and extract the binding energy using Eq. (70), i.e.,

$$\Delta = E_{\text{cont}}^{\min}(\mathbf{K}) - E_2(\mathbf{K}), \quad (91)$$

with $\Delta > 0$ denoting a state below the continuum. The dominant bound states occur mostly at $\mathbf{K} = \Gamma$, but re-

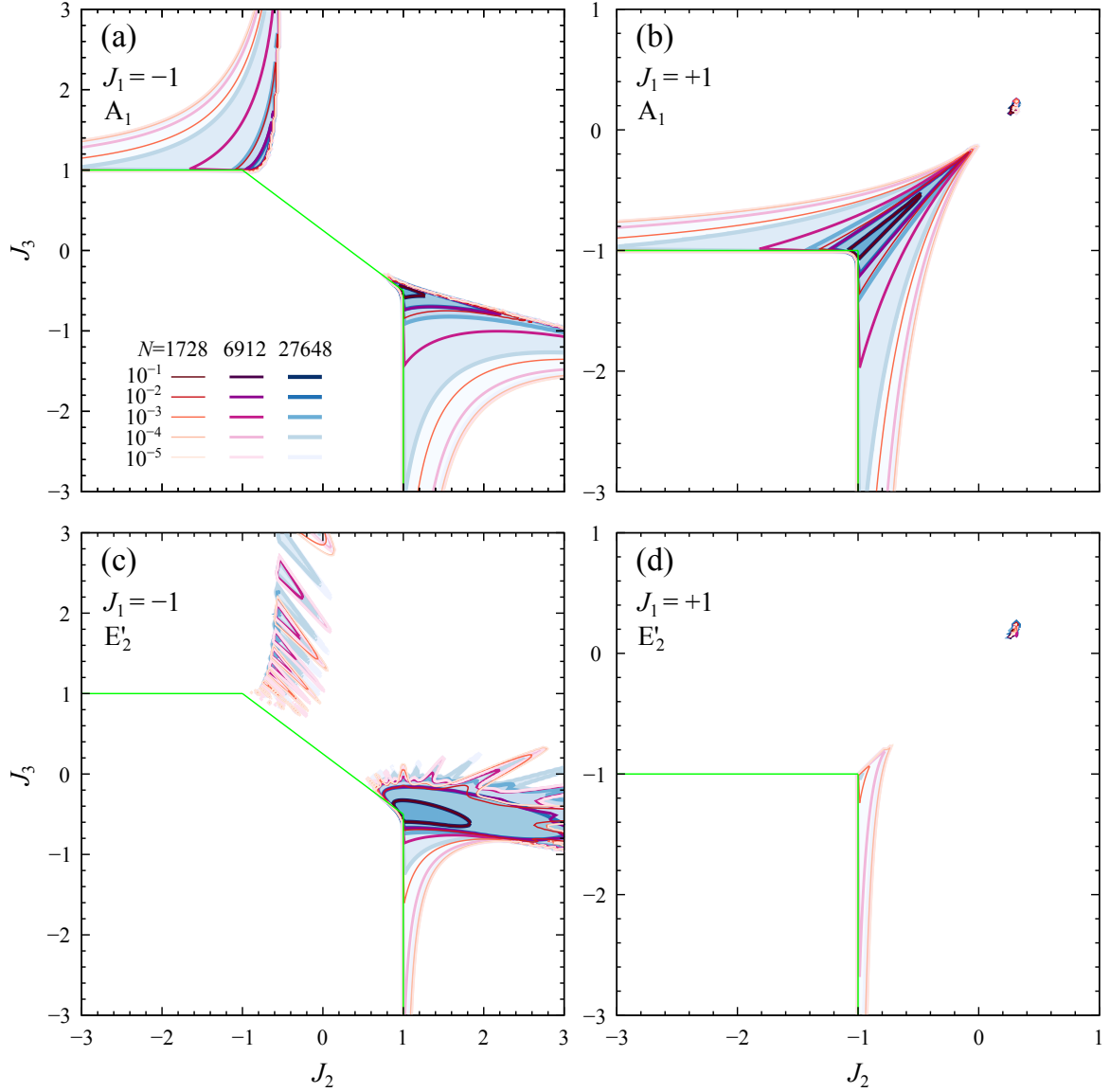


FIG. 7. The gap contours calculated from the $\mathbf{K} = 0$ gap equation (85) for $3 \times 24^2 = 1728$, and 6912, and 27648 site clusters in the A_1 [panels (a) and (b)] and in the E'_2 channels [panels (c) and (d)], both for $J_1 = 1$ and -1 . For larger values of the gap, the contours have converged, while for smaller values of the gap, the finite-size effects are large. There are considerable finite-size effects in the incommensurate phases, where the gap strongly oscillates. The largest value of the gap in the A_1 channel is for $(J_1, J_2, J_3) = (1, -1, -1)$ and in the E'_2 channel for $(-1, 1, -1/2)$. The green lines denote the boundary of the ferromagnetic phase.

gions with M -point and incommensurate total momentum also appear. The latter typically occur near regions where the one-magnon minima themselves are incommensurate. To understand this region better, one would need to extend the gap equation to include momenta beyond the Γ point.

The largest binding energies found in the present scan occur near two special parameter sets. For ferromagnetic nearest-neighbor exchange, the strongest binding appears at

$$(J_1, J_2, J_3) = (-1, 1, -1/2), \quad (92)$$

where the \mathcal{M}_{B_2} nodal-line minimum manifold is realized. For antiferromagnetic nearest-neighbor exchange, the largest A_1 -channel binding in the scanned region appears near

$$(J_1, J_2, J_3) = (1, -1, -1). \quad (93)$$

The representative finite-size energies are listed in Table I. In the first case the leading bound state is in the E_2 -type sector, while in the second case the leading state is in the fully symmetric A_1 sector. The small binding at $(J_1, J_2, J_3) = (-1, -1, 1)$ and the absence of a resolved gap at $(-1, 1/5, 1/10)$ provide useful checks that strong

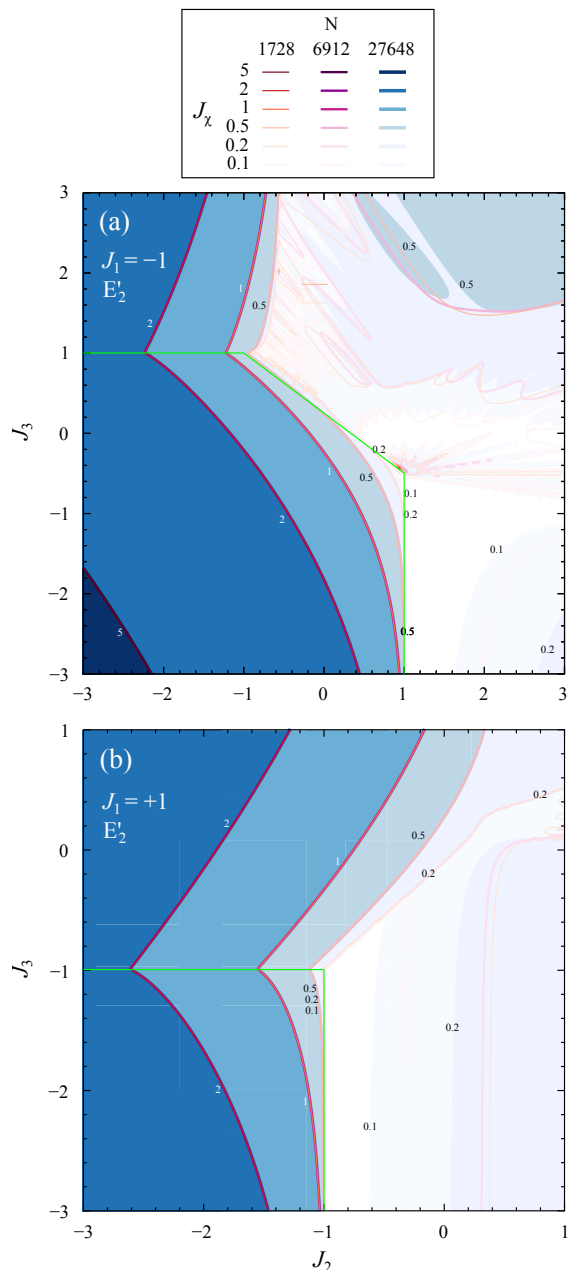


FIG. 8. The contour lines of the $|\Delta| = 10^{-4}$ gap for various values of J_χ . For both signs of J_1 , the chiral term greatly enhances the region of the two-magnon gap in the E'_2 symmetry channel. The green lines denote the boundary of the ferromagnetic phase.

frustration alone is not a sufficient predictor of a large two-magnon instability.

We next solve the $\mathbf{K} = 0$ gap equation in the symmetry-adapted partial-wave basis. Figure 7 shows the resulting gap contours in the A_1 and E_2 -type sectors for $N = 3 \times 24^2$, 3×48^2 , and 3×96^2 . The large-gap contours are already well converged with system size, while the small-gap contours show strong finite-size dependence. The finite-size effects are particularly

severe in the incommensurate regions, where the location of the continuum minimum changes sensitively with the discrete momentum mesh. We therefore regard the large-gap regions as robust, while the small-gap contours should be interpreted only qualitatively until a controlled finite-size scaling is performed - which is a nontrivial task for an exponentially small gap.

The partial-wave calculation confirms the channel structure suggested by the exact spectra. For $J_1 = -1$, the dominant Γ -point instability is in the E_2 -type sector and is strongest near the \mathcal{M}_{B_2} point. For $J_1 = +1$, the dominant large-gap region in the present scan is instead in the A_1 sector. This distinction is physically useful: it shows that the symmetry of the leading two-magnon bound state is not fixed solely by the triangular lattice, but depends sensitively on which frustrated manifold controls the low-energy one-magnon dispersion.

Finally, Fig. 8 shows the effect of a finite scalar-chirality coupling. Since the chirality term does not modify the one-magnon dispersion, the continuum edge is unchanged at fixed (J_1, J_2, J_3) . Its effect is instead entirely in the two-magnon interaction kernel. At $\mathbf{K} = 0$, this reduces to opposite shifts of the first-neighbor chiral couplings, as demonstrated by Eq. (87c). Consequently, J_χ splits the two opposite chiral components of the E_2 doublet and enhances binding in one of them, with the selected chirality determined by the sign of J_χ . The contours in Fig. 8 show that this effect can greatly enlarge the region where an E_2 -type two-magnon bound state is present. This is the central mechanism behind the chiral enhancement of two-magnon binding in the present model.

VII. CONCLUSION

We have studied two-magnon bound states above the fully polarized state of the spin-1/2 triangular-lattice J_1 - J_2 - J_3 Heisenberg model with an additional uniform scalar-chirality interaction. As a first step, we revisited the one-magnon sector of the Heisenberg model, which determines the ferromagnetic stability boundaries and the possible single-magnon instabilities. In this sector we identified two analytically tractable minimum manifolds by rewriting the one-magnon dispersion in complete-square form: the \mathcal{M}_{A_1} contour on the line $J_2 = 2J_3$, and the \mathcal{M}_{B_2} nodal-line manifold at $(J_1, J_2, J_3) = (-1, 1, -1/2)$. These complete-square decompositions make explicit the structure of the one-magnon minima studied in Ref. [51] and provide useful reference points for the two-magnon problem.

A central observation is that the uniform scalar-chirality term cancels exactly in the one-magnon sector. The oriented hopping amplitudes generated by the two bond-sharing triangles interfere destructively for a single flipped spin. Consequently, the chirality term leaves the one-magnon dispersion and the location of the single-magnon soft modes unchanged. This cancellation no

longer holds in the two-magnon sector: when two flipped spins occupy neighboring sites, the same oriented processes generate uncompensated amplitudes for the motion of the nearest-neighbor magnon pair. The scalar-chirality term therefore enters as a genuine two-magnon interaction. It can enhance pair binding without directly shifting the single-magnon instability, a role closely analogous in its effect to the enhancement produced by four-site ring exchange in related spin-nematic models [40, 55].

To test this mechanism, we derived two-magnon gap equations for the triangular lattice, following the strategy developed for the square lattice in Refs. [8, 12]. Using symmetry-adapted triangular-lattice harmonics, we reduced the $\mathbf{K} = 0$ problem to finite-dimensional gap equations in the A_1 and twofold-degenerate E_2 -type partial-wave sectors. At $\mathbf{K} = 0$, the scalar-chirality coupling splits the E_2 -type sector into two channels with opposite relative-motion chiralities. Their effective couplings are shifted linearly in J_χ ,

$$V_{1\pm} = \frac{3}{2}J_1 \pm 6\sqrt{3}J_\chi. \quad (94)$$

This splitting is the microscopic origin of the chiral enhancement of the two-magnon bound state. It is the main result of this work: a uniform scalar-chirality interaction, although invisible to the one-magnon spectrum, can selectively strengthen one chiral component of the two-magnon interaction and thereby increase the binding energy of a magnon pair.

Exact diagonalization in the two-magnon sector confirms the main features of the gap-equation analysis. The strongest binding in the ferromagnetic $J_1 = -1$ scan occurs near the \mathcal{M}_{B_2} point and belongs to the E_2 -type sector, whereas the strongest binding found for $J_1 = +1$ occurs in the A_1 sector near $(J_1, J_2, J_3) = (1, -1, -1)$. The enhanced binding near \mathcal{M}_{B_2} is consistent with the large low-energy density of two-magnon states generated by the nodal-line one-magnon minimum. In this respect, the triangular-lattice mechanism is analogous to the enhancement of two-magnon binding near degenerate one-magnon minima in the square-lattice J_1 - J_2 model [55, 60].

The relevance of these bound states to high-field spin nematics is controlled by the energy per flipped spin. A two-magnon bound state preempts ordinary magnon condensation only when $E_2(\mathbf{K})/2$ lies below the lowest one-magnon energy. If this condition is satisfied, the two-magnon bound state becomes gapless while the single-magnon excitation remains gapped. The natural instability below saturation is then toward a spin-nematic state with quadrupolar order parameter of the form $\langle S_i^- S_j^- \rangle$, rather than toward transverse dipolar magnetic order.

There are two important qualifications. First, the existence of a two-magnon bound state is not by itself sufficient to establish a stable spin-nematic phase. Bound states of three or more magnons may have a still lower energy per flipped spin, especially on the triangular lattice where triatic and higher multipolar orders are known

TABLE I. Energies for selected (J_1, J_2, J_3) parameter sets for the $N = 3 \times 24^2$ -site cluster from exact diagonalization. The E'_2 levels are twofold degenerate. The $E_{\text{cont}}^{\text{min}}(\mathbf{K})$ is the minimum of the two-magnon continuum.

| (J_1, J_2, J_3) | State | $E_{\text{cont}}^{\text{min}}(\mathbf{K})$ | Finite-size energy $N = 1728$ |
|-------------------|----------------|--|----------------------------------|
| $(1, -1, -1)$ | A_1 | 0 | -0.3124242152 |
| | E'_2 | | -0.0018259427 |
| $(-1, 1, -1/2)$ | E'_2 | 0 | -0.4386199066 |
| | A_1 | | -0.2993752450 |
| $(-1, -1, 1)$ | A_1 | 0 | -0.0171627324 |
| $(-1, 1/5, 1/10)$ | A_1 | 0 | 0 |
| $(-1, 1, 0)$ | M point | -4 | -4.0323521327 |
| | Γ point | -4 | -4.0021457564 |

to occur in related models. Second, the $\mathbf{K} = 0$ partial-wave gap equation does not capture bound states at M or at incommensurate total momentum. The exact-diagonalization scan shows that such states do occur in parts of the phase diagram. A complete high-field phase diagram therefore requires a momentum-resolved extension of the gap-equation approach, together with a comparison against higher-magnon sectors.

The main physical conclusion is that scalar chirality provides an efficient microscopic mechanism for enhancing two-magnon binding on the triangular lattice. Because it leaves the one-magnon spectrum unchanged while strengthening one chiral component of the two-magnon interaction, it can enlarge the parameter regime in which a two-magnon instability preempts single-magnon condensation. The scalar-chirality interaction therefore does more than perturb the two-magnon spectrum: it changes the symmetry selection of the bound state and provides a direct route by which a time-reversal-odd interaction can promote a time-reversal-even quadrupolar instability near saturation. A useful future direction would be to compare this mechanism systematically with the time-reversal-even four-site ring-exchange mechanism, since both can favor multipolar order while acting differently on the one- and two-magnon sectors.

ACKNOWLEDGMENTS

This work was supported by the National Research, Development and Innovation Office of Hungary (NKFIH) through OTKA Grant No. K 142652 and by the Doctoral Students' Excellence Program DKÖP-26-1-BME-28. This research was supported in part by the National

Science Foundation under Grant No. PHY-2309135 to the Kavli Institute for Theoretical Physics (KITP). We thank A. L. Chernyshev and J. Romhányi for discussions that led to this work, and N. Shannon for helpful discussions on spin-nematic physics.

Appendix A: The triangular lattice and the lattice harmonics

Our model describes spins on the triangular lattice illustrated in Fig. 1. The primitive vectors are

$$\mathbf{a}_1 = (1, 0), \quad \mathbf{a}_2 = \left(\frac{1}{2}, \frac{\sqrt{3}}{2} \right), \quad (\text{A1})$$

with lattice spacing set to unity. We define the first-neighbor bond vectors as

$$\begin{aligned} \delta_1^{(1)} &= -\delta_4^{(1)} = \mathbf{a}_1, \\ \delta_2^{(1)} &= -\delta_5^{(1)} = \mathbf{a}_2, \\ \delta_3^{(1)} &= -\delta_6^{(1)} = -\mathbf{a}_1 + \mathbf{a}_2, \end{aligned} \quad (\text{A2})$$

second-neighbor bond vectors as

$$\begin{aligned} \delta_1^{(2)} &= -\delta_4^{(2)} = -\mathbf{a}_1 + 2\mathbf{a}_2, \\ \delta_2^{(2)} &= -\delta_5^{(2)} = -2\mathbf{a}_1 + \mathbf{a}_2, \\ \delta_3^{(2)} &= -\delta_6^{(2)} = -\mathbf{a}_1 - \mathbf{a}_2, \end{aligned} \quad (\text{A3})$$

and the third-neighbor bond vectors as

$$\delta_j^{(3)} = 2\delta_j^{(1)}. \quad (\text{A4})$$

For each neighbor shell, we define symmetry-adapted lattice harmonics as Fourier sums over the corresponding bond vectors. The fully symmetric harmonics are

$$\gamma_{\mathbf{q}}^{(n)} = \frac{1}{6} \sum_{j=1}^6 e^{i\mathbf{q} \cdot \delta_j^{(n)}} \quad (\text{A5})$$

which gives

$$\gamma_{\mathbf{q}}^{(1)} = \frac{1}{3} \cos q_x + \frac{2}{3} \cos \frac{q_x}{2} \cos \frac{\sqrt{3}q_y}{2}, \quad (\text{A6a})$$

$$\gamma_{\mathbf{q}}^{(2)} = \frac{1}{3} \cos \sqrt{3}q_y + \frac{2}{3} \cos \frac{3q_x}{2} \cos \frac{\sqrt{3}q_y}{2}, \quad (\text{A6b})$$

$$\gamma_{\mathbf{q}}^{(3)} = \gamma_{2\mathbf{q}}^{(1)}. \quad (\text{A6c})$$

The fully symmetric harmonics transform according to the trivial A_1 irreducible representation of the D_6 point group. Each neighbor shell also contains harmonics transforming according to nontrivial irreducible representations. In particular, we use the following normalized E_2 cosine doublet to decompose the potential terms:

$$\gamma_{\mathbf{q}}^{(na)} = \frac{1}{3} \left(2 \cos \mathbf{q} \cdot \delta_1^{(n)} - \cos \mathbf{q} \cdot \delta_2^{(n)} - \cos \mathbf{q} \cdot \delta_3^{(n)} \right) \quad (\text{A7a})$$

$$\gamma_{\mathbf{q}}^{(nb)} = \frac{1}{\sqrt{3}} \left(\cos \mathbf{q} \cdot \delta_2^{(n)} - \cos \mathbf{q} \cdot \delta_3^{(n)} \right) \quad (\text{A7b})$$

Explicitly,

$$\begin{aligned} \gamma_{\mathbf{q}}^{(1a)} &= \frac{2}{3} \left(\cos q_x - \cos \frac{q_x}{2} \cos \frac{\sqrt{3}q_y}{2} \right), \\ \gamma_{\mathbf{q}}^{(2a)} &= \frac{2}{3} \left(\cos \sqrt{3}q_y - \cos \frac{3q_x}{2} \cos \frac{\sqrt{3}q_y}{2} \right), \\ \gamma_{\mathbf{q}}^{(3a)} &= \gamma_{2\mathbf{q}}^{(1a)}, \\ \gamma_{\mathbf{q}}^{(1b)} &= -\frac{2}{\sqrt{3}} \sin \frac{q_x}{2} \sin \frac{\sqrt{3}q_y}{2}, \\ \gamma_{\mathbf{q}}^{(2b)} &= \frac{2}{\sqrt{3}} \sin \frac{3q_x}{2} \sin \frac{\sqrt{3}q_y}{2}, \\ \gamma_{\mathbf{q}}^{(3b)} &= \gamma_{2\mathbf{q}}^{(1b)}, \end{aligned} \quad (\text{A8})$$

Here, $\gamma_{\mathbf{q}}^{(na)}$ and $\gamma_{\mathbf{q}}^{(nb)}$ denote the two components of the E_2 doublet in the n th neighbor shell. These symmetry-adapted lattice harmonics satisfy the decomposition identity

$$\gamma_{\mathbf{q}+\mathbf{p}}^{(n)} + \gamma_{\mathbf{q}-\mathbf{p}}^{(n)} = 2\gamma_{\mathbf{q}}^{(n)}\gamma_{\mathbf{p}}^{(n)} + \gamma_{\mathbf{q}}^{(na)}\gamma_{\mathbf{p}}^{(na)} + \gamma_{\mathbf{q}}^{(nb)}\gamma_{\mathbf{p}}^{(nb)}. \quad (\text{A9})$$

For channel decoupling in the chiral phase, it is convenient to introduce the chiral E_2 combinations

$$\gamma_{\mathbf{q}}^{(n\pm)} = \gamma_{\mathbf{q}}^{(na)} \pm i\gamma_{\mathbf{q}}^{(nb)}. \quad (\text{A10})$$

Equivalently,

$$\begin{aligned} \gamma_{\mathbf{q}}^{(n\pm)} &= \frac{1}{3} \sum_{j=1}^6 e^{\pm 2i(j-1)\pi/3} e^{i\mathbf{q} \cdot \delta_j^{(n)}} \\ &= \gamma_{\mathbf{q}}^{(na)} \pm i\gamma_{\mathbf{q}}^{(nb)}. \end{aligned} \quad (\text{A11})$$

The decomposition rule is now

$$\gamma_{\mathbf{q}+\mathbf{p}}^{(n)} + \gamma_{\mathbf{q}-\mathbf{p}}^{(n)} = 2\gamma_{\mathbf{q}}^{(n)}\gamma_{\mathbf{p}}^{(n)} + \frac{1}{2}\bar{\gamma}_{\mathbf{q}}^{(n-)}\gamma_{\mathbf{p}}^{(n-)} + \frac{1}{2}\bar{\gamma}_{\mathbf{q}}^{(n+)}\gamma_{\mathbf{p}}^{(n+)}. \quad (\text{A12})$$

Appendix B: Auxiliary-space derivation of the chiral two-magnon kernel

This appendix gives the technical derivation of the scalar-chirality contribution to the two-magnon interaction kernel. The purpose of the derivation is to isolate the genuine two-magnon interaction from the free propagation of two independent spin flips while keeping the spin-1/2 hard-core constraint explicit.

We first enlarge the physical two-magnon Hilbert space of the $S = 1/2$ spins by adjoining auxiliary double-occupancy states. The enlarged space is the direct sum

$$\mathcal{H}_{2X} = \mathcal{H}_{2R} \oplus \mathcal{H}_{2D}, \quad (\text{B1})$$

where

$$\mathcal{H}_{2R} = \{|i, j\rangle \mid i \neq j\}, \quad |i, j\rangle = \hat{S}_j^- \hat{S}_i^- |\text{FM}\rangle, \quad (\text{B2})$$

and

$$\mathcal{H}_{2D} = \{|j, j\rangle \mid j = 1, \dots, N\}. \quad (\text{B3})$$

The states $|j, j\rangle$ are not physical spin-1/2 states. They are introduced only as auxiliary bookkeeping states that allow the free two-particle propagation to be defined before the hard-core projection is imposed.

At fixed total momentum \mathbf{K} , we use

$$|\mathbf{K}, \mathbf{q}\rangle_{\text{R}} = \frac{1}{2N} \sum_{i \neq j} e^{-i\frac{\mathbf{K}}{2} \cdot (\mathbf{r}_i + \mathbf{r}_j)} e^{-i\mathbf{q} \cdot (\mathbf{r}_j - \mathbf{r}_i)} |i, j\rangle, \quad (\text{B4})$$

and the auxiliary double-occupancy state

$$|\mathbf{K}\rangle_{\text{D}} = \sum_{j=1}^N e^{-i\mathbf{K} \cdot \mathbf{r}_j} |j, j\rangle. \quad (\text{B5})$$

The enlarged momentum state is

$$|\mathbf{K}, \mathbf{q}\rangle_{\text{X}} = |\mathbf{K}, \mathbf{q}\rangle_{\text{R}} \oplus |\mathbf{K}\rangle_{\text{D}}. \quad (\text{B6})$$

The physical projection is

$$\hat{\mathcal{P}}_{2\text{R}} = \hat{\mathbf{1}}_{2\text{X}} - \sum_i |i, i\rangle \langle i, i|. \quad (\text{B7})$$

We define the free two-magnon Hamiltonian \hat{H}_0 in the enlarged space by

$$\hat{H}_0 |\mathbf{K}, \mathbf{q}\rangle_{\text{X}} = \left(\varepsilon_{\frac{\mathbf{K}}{2} + \mathbf{q}} + \varepsilon_{\frac{\mathbf{K}}{2} - \mathbf{q}} \right) |\mathbf{K}, \mathbf{q}\rangle_{\text{X}}. \quad (\text{B8})$$

Equivalently, in real space this operator acts independently on the two spin-flip coordinates before the hard-core projection is imposed. The interaction is obtained from the projected difference

$$\hat{V} = \hat{\mathcal{P}}_{2\text{R}} \left(\hat{H} - \hat{H}_0 \right) \hat{\mathcal{P}}_{2\text{R}}. \quad (\text{B9})$$

With this convention the projected Schrödinger equation in the regular sector has the form

$$\left[E_2 - \varepsilon_{\frac{\mathbf{K}}{2} + \mathbf{q}} - \varepsilon_{\frac{\mathbf{K}}{2} - \mathbf{q}} \right] \psi_{\mathbf{K}}^{\text{R}}(\mathbf{q}) = \frac{1}{N} \sum_{\mathbf{p}} V_{\mathbf{K}}(\mathbf{q}, \mathbf{p}) \psi_{\mathbf{K}}^{\text{R}}(\mathbf{p}). \quad (\text{B10})$$

For the scalar-chirality term the projected interaction can be evaluated directly in the configuration basis. Using

$$4\hat{\chi}_{ijk} = i\hat{P}_{ijk} - i\hat{P}_{ikj}, \quad (\text{B11})$$

each oriented triangle contributes an imaginary amplitude whose sign is fixed by the orientation of the cyclic permutation. The terms that cancel in the one-magnon sector no longer cancel pairwise in the two-magnon sector. Carrying out the action of $\hat{\mathcal{P}}_{2\text{R}}(\hat{H}_{\text{Chir}} - \hat{H}_{0, \text{Chir}})\hat{\mathcal{P}}_{2\text{R}}$ on $|\mathbf{K}, \mathbf{q}\rangle_{\text{R}}$, and Fourier transforming back to the relative momentum \mathbf{p} , gives

$$V_{\mathbf{K}}^{(\text{X})}(\mathbf{q}, \mathbf{p}) = -i12\sqrt{3}J_{\text{X}} \left[\gamma_{\mathbf{p}}^{(1)} \left(\gamma_{\frac{\mathbf{K}}{2}}^{(1a)} \gamma_{\mathbf{q}}^{(1b)} - \gamma_{\frac{\mathbf{K}}{2}}^{(1b)} \gamma_{\mathbf{q}}^{(1a)} \right) + \gamma_{\mathbf{p}}^{(1a)} \left(\gamma_{\frac{\mathbf{K}}{2}}^{(1b)} \gamma_{\mathbf{q}}^{(1)} - \gamma_{\frac{\mathbf{K}}{2}}^{(1)} \gamma_{\mathbf{q}}^{(1b)} \right) + \gamma_{\mathbf{p}}^{(1b)} \left(\gamma_{\frac{\mathbf{K}}{2}}^{(1)} \gamma_{\mathbf{q}}^{(1a)} - \gamma_{\frac{\mathbf{K}}{2}}^{(1a)} \gamma_{\mathbf{q}}^{(1)} \right) \right]. \quad (\text{B12})$$

Here $\gamma^{(1)}$, $\gamma^{(1a)}$, and $\gamma^{(1b)}$ are the first-neighbor triangular-lattice harmonics defined in the main text or in Appendix A. The antisymmetric structure in the brackets reflects the orientation of the scalar-chirality interaction.

It is more transparent to rewrite Eq. (B12) in the complex C_6 harmonic basis. Using the relations between the real and complex first-neighbor harmonics, one obtains

$$V_{\mathbf{K}}^{(\text{X})}(\mathbf{q}, \mathbf{p}) = -6\sqrt{3}J_{\text{X}} \left[\gamma_{\frac{\mathbf{K}}{2}}^{(1)} \left(\gamma_{\mathbf{p}}^{(1-)*} \gamma_{\mathbf{q}}^{(1-)} - \gamma_{\mathbf{p}}^{(1+)*} \gamma_{\mathbf{q}}^{(1+)} \right) + \gamma_{\frac{\mathbf{K}}{2}}^{(1+)} \left(\gamma_{\mathbf{p}}^{(1+)*} \gamma_{\mathbf{q}}^{(1)} - \gamma_{\mathbf{p}}^{(1)*} \gamma_{\mathbf{q}}^{(1-)} \right) + \gamma_{\frac{\mathbf{K}}{2}}^{(1-)} \left(\gamma_{\mathbf{p}}^{(1)*} \gamma_{\mathbf{q}}^{(1+)} - \gamma_{\mathbf{p}}^{(1-)*} \gamma_{\mathbf{q}}^{(1)} \right) \right]. \quad (\text{B13})$$

This is the form used in the partial-wave reduction of the two-magnon Schrödinger equation. It explicitly shows that the scalar-chirality interaction couples first-neighbor lattice-harmonic channels via oriented, time-reversal-odd amplitudes. The full kernel is

$$V_{\mathbf{K}}(\mathbf{q}, \mathbf{p}) = V_{\mathbf{K}}^{(\text{H})}(\mathbf{q}, \mathbf{p}) + V_{\mathbf{K}}^{(\text{X})}(\mathbf{q}, \mathbf{p}), \quad (\text{B14})$$

where $V_{\mathbf{K}}^{(\text{H})}$ is the Heisenberg contribution.

-
- [1] M. Blume and Y. Y. Hsieh, Biquadratic exchange and quadrupolar ordering, *J. Appl. Phys.* **40**, 1249 (1969); A. F. Andreev and I. A. Grishchuk, Spin nematics, *Sov. Phys. JETP* **60**, 267 (1984).
 [2] K. Penc and A. M. Läuchli, Spin Nematic Phases in Quantum Spin Systems, in *Introduction to Frustrated Magnetism: Materials, Experiments, Theory*, edited by C. Lacroix, P. Mendels, and F. Mila (Springer-Verlag

- Berlin Heidelberg, 2011) p. 331.
 [3] A. V. Chubukov, Chiral, nematic, and dimer states in quantum spin chains, *Phys. Rev. B* **44**, 4693 (1991).
 [4] V. Zapf, M. Jaime, and C. D. Batista, Bose-einstein condensation in quantum magnets, *Rev. Mod. Phys.* **86**, 563 (2014).
 [5] R. O. Kuzian and S.-L. Drechsler, Exact one- and two-particle excitation spectra of acute-angle helimagnets

- above their saturation magnetic field, *Phys. Rev. B* **75**, 024401 (2007).
- [6] T. Hikihara, L. Kecke, T. Momoi, and A. Furusaki, Vector chiral and multipolar orders in the spin- $\frac{1}{2}$ frustrated ferromagnetic chain in magnetic field, *Phys. Rev. B* **78**, 144404 (2008).
- [7] J. Sudan, A. Lüscher, and A. M. Läuchli, Emergent multipolar spin correlations in a fluctuating spiral: The frustrated ferromagnetic spin-1/2 Heisenberg chain in a magnetic field, *Phys. Rev. B* **80**, 140402(R) (2009).
- [8] M. E. Zhitomirsky and H. Tsunetsugu, Magnon pairing in quantum spin nematic, *Europhysics Letters* **92**, 37001 (2010).
- [9] L. Balents and O. A. Starykh, Quantum Lifshitz field theory of a frustrated ferromagnet, *Phys. Rev. Lett.* **116**, 177201 (2016).
- [10] N. Shannon, T. Momoi, and P. Sindzingre, Nematic Order in Square Lattice Frustrated Ferromagnets, *Phys. Rev. Lett.* **96**, 027213 (2006).
- [11] Y. Iqbal, P. Ghosh, R. Narayanan, B. Kumar, J. Reuther, and R. Thomale, Intertwined nematic orders in a frustrated ferromagnet, *Phys. Rev. B* **94**, 224403 (2016).
- [12] S. Jiang, J. Romhányi, S. R. White, M. E. Zhitomirsky, and A. L. Chernyshev, Where is the quantum spin nematic?, *Phys. Rev. Lett.* **130**, 116701 (2023), [arXiv:2209.00010 \[cond-mat.str-el\]](https://arxiv.org/abs/2209.00010).
- [13] F. Mila, Closing in on a Magnetic Analog of Liquid Crystals, *Physics* **10**, 64 (2017).
- [14] R. Nath, A. A. Tsirlin, H. Rosner, and C. Geibel, Magnetic properties of $\text{BaCdVO}(\text{PO}_4)_2$: A strongly frustrated spin- $\frac{1}{2}$ square lattice close to the quantum critical regime, *Phys. Rev. B* **78**, 064422 (2008).
- [15] L. E. Svistov, T. Fujita, H. Yamaguchi, S. Kimura, K. Omura, A. Prokofiev, A. I. Smirnov, Z. Honda, and M. Hagiwara, New high magnetic field phase of the frustrated $S=1/2$ chain compound LiCuVO_4 , *JETP letters* **93**, 21 (2011).
- [16] A. Orlova, E. L. Green, J. M. Law, D. I. Gorbunov, G. Chanda, S. Krämer, M. Horvatić, R. K. Kremer, J. Wosnitza, and G. L. J. A. Rikken, Nuclear magnetic resonance signature of the spin-nematic phase in LiCuVO_4 at high magnetic fields, *Phys. Rev. Lett.* **118**, 247201 (2017).
- [17] M. Yoshida, K. Nawa, H. Ishikawa, M. Takigawa, M. Jeong, S. Krämer, M. Horvatić, C. Berthier, K. Matsui, T. Goto, S. Kimura, T. Sasaki, J. Yamaura, H. Yoshida, Y. Okamoto, and Z. Hiroi, Spin dynamics in the high-field phases of volborthite, *Phys. Rev. B* **96**, 180413(R) (2017).
- [18] Y. Kohama, H. Ishikawa, A. Matsuo, K. Kindo, N. Shannon, and Z. Hiroi, Possible observation of quantum spin-nematic phase in a frustrated magnet, *Proc. Natl. Acad. Sci. U.S.A.* **116**, 10686 (2019).
- [19] K. Y. Povarov, V. K. Bhartiya, Z. Yan, and A. Zheludev, Thermodynamics of a frustrated quantum magnet on a square lattice, *Phys. Rev. B* **99**, 024413 (2019).
- [20] V. K. Bhartiya, K. Y. Povarov, D. Blosser, S. Bettler, Z. Yan, S. Gvasaliya, S. Raymond, E. Ressouche, K. Beauvois, J. Xu, F. Yokaichiya, and A. Zheludev, Presaturation phase with no dipolar order in a quantum ferro-antiferromagnet, *Phys. Rev. Research* **1**, 033078 (2019).
- [21] F. Landolt, S. Bettler, Z. Yan, S. Gvasaliya, A. Zheludev, S. Mishra, I. Sheikin, S. Krämer, M. Horvatić, A. Gazizulina, and O. Prokhnenko, Presaturation phase in the frustrated ferro-antiferromagnet $\text{Pb}_2\text{VO}(\text{PO}_4)_2$, *Phys. Rev. B* **102**, 094414 (2020).
- [22] K. M. Ranjith, F. Landolt, S. Raymond, A. Zheludev, and M. Horvatić, NMR evidence against a spin-nematic nature of the presaturation phase in the frustrated magnet $\text{SrZnVO}(\text{PO}_4)_2$, *Phys. Rev. B* **105**, 134429 (2022).
- [23] D. Flavián, S. Hayashida, L. Huberich, D. Blosser, K. Y. Povarov, Z. Yan, S. Gvasaliya, and A. Zheludev, Magnetic phase diagram of the linear quantum ferro-antiferromagnet $\text{Cs}_2\text{Cu}_2\text{Mo}_3\text{O}_{12}$, *Phys. Rev. B* **101**, 224408 (2020).
- [24] R. K. Kaul, Spin nematic ground state of the triangular lattice $s = 1$ biquadratic model, *Phys. Rev. B* **86**, 104411 (2012).
- [25] A. Völl and S. Wessel, Spin dynamics of the bilinear-biquadratic $s = 1$ heisenberg model on the triangular lattice: A quantum monte carlo study, *Phys. Rev. B* **91**, 165128 (2015).
- [26] A. Smerald and N. Shannon, Theory of spin excitations in a quantum spin-nematic state, *Phys. Rev. B* **88**, 184430 (2013).
- [27] B. S. Shastry and B. I. Shraiman, Theory of raman scattering in mott-hubbard systems, *Phys. Rev. Lett.* **65**, 1068 (1990).
- [28] F. Michaud, F. Vernay, and F. Mila, Theory of inelastic light scattering in spin-1 systems: Resonant regimes and detection of quadrupolar order, *Phys. Rev. B* **84**, 184424 (2011).
- [29] W.-H. Ko, Z.-X. Liu, T.-K. Ng, and P. A. Lee, Raman signature of the $u(1)$ dirac spin-liquid state in the spin- $\frac{1}{2}$ kagome system, *Phys. Rev. B* **81**, 024414 (2010).
- [30] L. Savary and T. Senthil, Probing hidden orders with resonant inelastic x-ray scattering (2015), [arXiv:1506.04752 \[cond-mat.str-el\]](https://arxiv.org/abs/1506.04752).
- [31] A. Nag, A. Nocera, S. Agrestini, M. Garcia-Fernandez, A. C. Walters, S.-W. Cheong, S. Johnston, and K.-J. Zhou, Quadrupolar magnetic excitations in an isotropic spin-1 antiferromagnet, *Nature Communications* **13**, 2327 (2022).
- [32] H. Kim, J.-K. Kim, J. Kwon, J. Kim, H.-W. J. Kim, S. Ha, K. Kim, W. Lee, J. Kim, G. Y. Cho, H. Heo, J. Jang, C. J. Sahle, A. Longo, J. Stremper, G. Fabbris, Y. Choi, D. Haskel, J. Kim, J. W. Kim, and B. J. Kim, Quantum spin nematic phase in a square-lattice iridate, *Nature* **625**, 264 (2024).
- [33] T. Arima, Ferroelectricity induced by proper-screw type magnetic order, *Journal of the Physical Society of Japan* **76**, 073702 (2007), <https://doi.org/10.1143/JPSJ.76.073702>.
- [34] M. Akaki, D. Yoshizawa, A. Okutani, T. Kida, J. Romhányi, K. Penc, and M. Hagiwara, Direct observation of spin-quadrupolar excitations in $\text{Sr}_2\text{CoGe}_2\text{O}_7$ by high-field electron spin resonance, *Phys. Rev. B* **96**, 214406 (2017).
- [35] V. Kalmeyer and R. B. Laughlin, Equivalence of the resonating-valence-bond and fractional quantum hall states, *Phys. Rev. Lett.* **59**, 2095 (1987); X. G. Wen, F. Wilczek, and A. Zee, Chiral spin states and superconductivity, *Phys. Rev. B* **39**, 11413 (1989).
- [36] A. Wietek and A. M. Läuchli, Chiral spin liquid and quantum criticality in extended $s = 1/2$ heisenberg models on the triangular lattice, *Phys. Rev. B* **95**, 035141 (2017), [arXiv:1604.07829 \[cond-mat.str-el\]](https://arxiv.org/abs/1604.07829).

- [37] A. Szasz, J. Motruk, M. P. Zaletel, and J. E. Moore, Chiral spin liquid phase of the triangular lattice hubbard model: A density matrix renormalization group study, *Phys. Rev. X* **10**, 021042 (2020), arXiv:1808.00463 [cond-mat.str-el].
- [38] B.-B. Chen, Z. Chen, S.-S. Gong, D. N. Sheng, W. Li, and A. Weichselbaum, Quantum spin liquid with emergent chiral order in the triangular-lattice hubbard model, *Phys. Rev. B* **106**, 094420 (2022), arXiv:2102.05560 [cond-mat.str-el].
- [39] T. Cookmeyer, J. Motruk, and J. E. Moore, Four-spin terms and the origin of the chiral spin liquid in mott insulators on the triangular lattice, *Phys. Rev. Lett.* **127**, 087201 (2021), arXiv:2103.07438 [cond-mat.str-el].
- [40] T. Momoi, P. Sindzingre, and N. Shannon, Octupolar order in the multiple spin exchange model on a triangular lattice, *Phys. Rev. Lett.* **97**, 257204 (2006), arXiv:cond-mat/0611575.
- [41] T. Momoi, P. Sindzingre, and K. Kubo, Spin nematic order in multiple-spin exchange models on the triangular lattice, *Phys. Rev. Lett.* **108**, 057206 (2012), arXiv:1107.5501 [cond-mat.str-el].
- [42] A. Läuchli, F. Mila, and K. Penc, Quadrupolar phases of the $s = 1$ bilinear-biquadratic heisenberg model on the triangular lattice, *Phys. Rev. Lett.* **97**, 087205 (2006).
- [43] H. Tsunetsugu and M. Arikawa, Spin nematic phase in $s=1$ triangular antiferromagnets, *Journal of the Physical Society of Japan* **75**, 083701 (2006), <https://doi.org/10.1143/JPSJ.75.083701>.
- [44] S. Bhattacharjee, V. B. Shenoy, and T. Senthil, Possible ferro-spin nematic order in NiGa_2S_4 , *Phys. Rev. B* **74**, 092406 (2006).
- [45] S. Nakatsuji, Y. Nambu, H. Tonomura, O. Sakai, S. Jonas, C. Broholm, H. Tsunetsugu, Y. Qiu, and Y. Maeno, Spin disorder on a triangular lattice, *Science* **309**, 1697 (2005), <https://www.science.org/doi/pdf/10.1126/science.1114727>.
- [46] J. Sheng, J.-W. Mei, L. Wang, X. Xu, W. Jiang, L. Xu, H. Ge, N. Zhao, T. Li, A. Candini, B. Xi, J. Zhao, Y. Fu, J. Yang, Y. Zhang, G. Biasiol, S. Wang, J. Zhu, P. Miao, X. Tong, D. Yu, R. Mole, Y. Cui, L. Ma, Z. Zhang, Z. Ouyang, W. Tong, A. Podlesnyak, L. Wang, F. Ye, D. Yu, W. Yu, L. Wu, and Z. Wang, Bose-einstein condensation of a two-magnon bound state in a spin-1 triangular lattice, *Nature Materials* **24**, 544 (2025).
- [47] J. Sheng, J. Hu, L. Xu, L. Wang, X. Shi, R. Chi, D. Yu, A. Podlesnyak, P. Piyawongwatthana, N. Murai, S. Ohira-Kawamura, H. Yuan, L. Wang, J.-W. Mei, H.-J. Liao, T. Xiang, L. Wu, and Z. Wang, Possible observation of quadrupole waves in spin nematics, *Phys. Rev. Lett.* **135**, 156704 (2025).
- [48] O. I. Motrunich, Orbital magnetic field effects in spin liquid with spinon fermi sea: Possible application to $\kappa\text{-(et)}_2\text{Cu}_2(\text{cn})_3$, *Phys. Rev. B* **73**, 155115 (2006).
- [49] L. N. Bulaevskii, C. D. Batista, M. V. Mostovoy, and D. I. Khomskii, Electronic orbital currents and polarization in mott insulators, *Phys. Rev. B* **78**, 024402 (2008).
- [50] L. Messio, C. Lhuillier, and G. Misguich, Lattice symmetries and regular magnetic orders in classical frustrated antiferromagnets, *Phys. Rev. B* **83**, 184401 (2011).
- [51] M. Mohylina, F. A. Gómez Albarracín, M. Žukovič, and H. D. Rosales, Spontaneous antiferromagnetic skyrmion/antiskyrmion lattice and spiral spin-liquid states in the frustrated triangular lattice, *Phys. Rev. B* **106**, 224406 (2022).
- [52] T. Okubo, S. Chung, and H. Kawamura, Multiple- q states and the skyrmion lattice of the triangular-lattice heisenberg antiferromagnet under magnetic fields, *Phys. Rev. Lett.* **108**, 017206 (2012).
- [53] A. O. Leonov and M. Mostovoy, Multiply periodic states and isolated skyrmions in an anisotropic frustrated magnet, *Nature Communications* **6**, 8275 (2015).
- [54] P. Balla, Y. Iqbal, and K. Penc, Affine lattice construction of spiral surfaces in frustrated heisenberg models, *Phys. Rev. B* **100**, 140402 (2019).
- [55] N. Shannon, T. Momoi, and P. Sindzingre, Nematic order in square lattice frustrated ferromagnets, *Phys. Rev. Lett.* **96**, 027213 (2006).
- [56] M. Wortis, Bound States of Two Spin Waves in The Heisenberg Ferromagnet, *Phys. Rev.* **132**, 85 (1963).
- [57] J. Hanus, Bound states in the heisenberg ferromagnet, *Phys. Rev. Lett.* **11**, 336 (1963).
- [58] D. C. Mattis, *The Theory of Magnetism Made Simple: An Introduction to Physical Concepts and to Some Useful Mathematical Methods* (World Scientific, Singapore, 2006).
- [59] T. Momoi and N. Shannon, Nematic Order in the Multiple-Spin Exchange Model on the Triangular Lattice, *Prog. Theor. Phys.* **159**, 72 (2005).
- [60] N. Shannon, B. Schmidt, K. Penc, and P. Thalmeier, Finite temperature properties and frustrated ferromagnetism in a square lattice heisenberg model, *The European Physical Journal B - Condensed Matter and Complex Systems* **38**, 599 (2004).